Structural and functional studies of causative factors for infectious diseases

(感染症の原因となるタンパク質の構造生物学的研究)

Toshiharu TSURUMURA

Kyoto Sangyo University

2014

Preface

The studies presented here have been carried out under the Professor Hideaki TSUGE, at Faculty of Home Economics, Tokushima Bunri University in 2004 and Faculty of Life Sciences, Kyoto Sangyo University from 2010 to now, in Japan.

The object of the thesis is X-ray structural analyses of three proteins to reveal their structure-function relationships and interactions with substrate proteins or ligands.

Toshiharu TSURUMURA

Department of Bioresource and Environmental Sciences,
Faculty of Life Sciences, Kyoto Sangyo University

October, 2014

Table of Contents

General Introduction 1

Chapter I:
Conformational change of carcinogenic factor TNF-α inducing protein from *Helicobacter pylori* for gastric cancer progression 10

I.1 Introduction 10

I.2 Materials and Methods 11

I.2.1 Sample preparation and crystallization of del-Tipα

I.2.2 Data collection and model building

I.2.3 Circular dichroism measurement

I.3 Results and Discussions 13

I.3.1 Overall structure of del-Tipα

I.3.2 Quaternary structure of del-Tipα

I.3.3 Structural similarity between Tipα and del-Tipα in solution

I.3.4 Conformational change of Tipα and del-Tipα

Chapter II:
Initial action of cap snatching mechanism of Influenza RNA polymerase 22

II.1 Introduction 22

II.2 Materials and Methods 23

II.2.1 Sample preparation and crystallization of PB2 middle domain

II.2.2 Data collection and model building

II.3 Results 24

II.3.1 Properties of the middle domain of PB2 (H1N1)

II.3.2 Structure of the H1N1 PB2 middle domain

II.3.3 Conformational polymorphism of m^7GTP

II.4 Discussion 29

Chapter III
Arginine ADP-ribosylation mechanism of iota-toxin from *Clostridium perfringens* 37

III.1 Introduction 37

III.2 Materials and Methods 38

III.2.1 Sample preparation, crystallization, and NAD^+ soaking

III.2.2 Data collection and model building

III.2.3 Assay of ARTase and NADase Activity

III.3 Results 41

III.3.1 Structures of Ia-Actin complexes

III.3.2 Plasticity of the ARTT loop within the complex upon ADP-ribosylation

III.3.3 Reaction mechanism inferred from the structures

III.4 Discussion 49

Conclusion 57

References 59

List of publications 65

Acknowledgement 67

Abbreviations

Chapter I

CagA:	cytotoxin-associated antigen
cagPAI:	cag pathogenicity island
CD:	circular dichroism
FAD:	flavin adenine dinucleotide
HP-MP1:	*H. pylori*-membrane protein 1
IL:	interleukin
PBP:	penicillin-binding protein
Tipα:	TNF-αinducing protein
TNF-α:	tumor necrosis factor α
VacA:	vacuolating cytotoxin

Chapter II

$CC_{1/2}$:	Pearson correlation coefficient half
EDA-m^7GTP:	2'/3'-O-(2-Aminoethyl-carbamoyl)-7-methyl-guanosine -5'-triphosphate
GTP:	guanosine triphosphate
GTPγS:	guanosine 5'-O-(3-thiotriphosphate)
HxNy:	combination of haemagglutinin and neuraminidase
m^7G:	7-methyl-guanosine
m^7GDP:	7-methyl-guanosine-5'-diphosphate
m^7GMP:	7-methyl-guanosine-5'-monophosphate
m^7GTP:	7-methyl-guanosine-5'-triphosphate
m^7GP5G:	P1-(5'-7-Methyl-Guanosyl)-P5-(5'-Guanosyl)-pentaphosphate
NLS:	nuclear localization signal
NP:	nucleoprotein
PA:	polymerase acidic protein
PB1:	polymerase basic protein 1
PB2:	polymerase basic protein 2
RNP:	ribonucleopotein

Chapter III

ADPR:	ADP-ribosylated
ART:	ADP-ribosyl transferase
ARTT:	ADP-ribosylating toxin turn-turn
ϐTAD:	thiazole-4-carboxamide adenine dinucleotide
C2I:	enzymatic subunit of C2 toxin from *Clostridium botulinum*
C2II:	membrane transporting subunit of C2 toxin from *Clostridium botulinum*
C3, C3bot:	C3 exotoxin from *Clostridium botulinum*
C3lim:	C3 exotoxin from *Clostridium limosum*

C3stau:	C3 exotoxin from *Staphylococcus aureus*
CDTa:	enzymatic subunit of CD toxin from *Clostridium difficile*
eEF2:	elongation factor 2
ExoA:	exotoxin A
Ia:	enzymatic subunit of iota toxin from *Clostridium perfringens*
Ib:	membrane transporting subunit of iota toxin from *Clostridium perfringens*
NMN:	nicotinamide mononucleotide
SpvB:	*Salmonella enterica* virulence-associated protein
VahC:	virulence factor from *Aeromonas hydrophila*
VIP2:	vegetative insecticidal protein

General Introduction

This study focuses on three proteins, which are associated with infectious diseases: I) tumor necrosis factor (TNF)-α-inducing protein (Tipα) from *Helicobacter pylori;* II) the PB2 subunit of RNA polymerase from Influenza A virus (H1N1); III) the toxic subunit of Iota toxin (Ia) from *Clostridium perfringens*.

Infection is defined as the invasion of microorganisms into the living host, and it elicits an immune response in the host. Infectious diseases are caused by pathogenic microorganisms, such as bacteria, viruses, and parasites. The diseases can spread from one person to another, directly or indirectly. Because of the pathogenicity of the pathogenic microorganisms, they are able to survive in the host cells by disrupting the mechanism of transcription and replication or utilizing nutrients from their host cells. The pathogens interact with the target host proteins or nucleotides (or other cellular contents), and the host factors lose their activities[1,2]. There are several classifications on the basis of the properties of pathogenic microorganisms or symptoms, infection terms, and so on. The classifications in bacterial and viral infections are described as follows:

Infectious diseases by bacteria are grouped by their pathogenicity, such as invasiveness, toxigenicity, infectivity, into the following three categories: i) toxin-related illness, ii) exudative inflammation illness, and iii) proliferative inflammation illness (Figure 1)[1,2]. Two proteins in this study, Tipα from *H. pylori* and Ia from *C. perfringens*, are included in toxin-related illness, because they are toxins secreted by bacteria, which induce cell

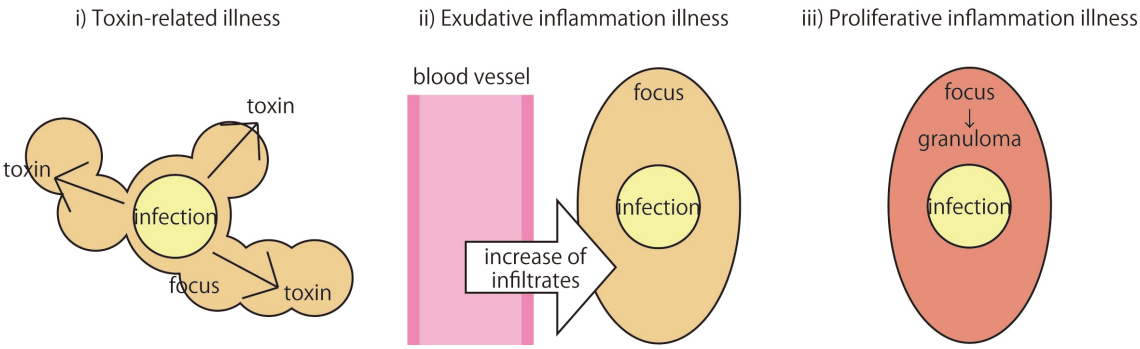

Figure 1 Classification of bacteria infection. i) Toxin-related illness; this is caused by the toxins produced by pathogenic bacteria such as *Corynebacterium diphtheria* and *Vibrio cholera*. ii) Exudative inflammation illness; bacteria propagate around the spot of infection, causing exudative inflammation such as genus *Staphylococcus*, genus *Streptococcus* and *Shigella*. iii) Proliferative inflammation illness; bacteria cause proliferative inflammation and granulomatous inflammation in the whole body via lymph node after infection.

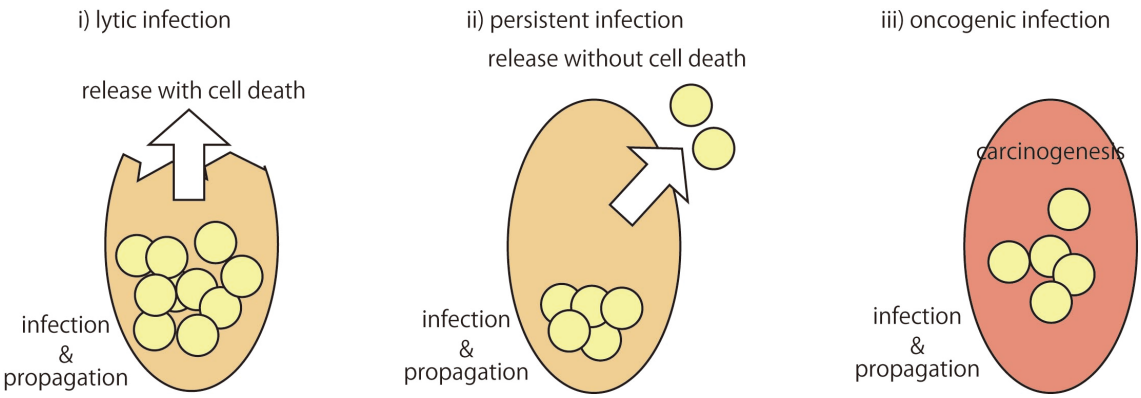

Figure 2 Classification of virus infection. i) lytic infection; after infection of bacteria into the cells and propagation of them, many progeny are released out of cells with cytopathogenic effect. ii) persistent infection; infected virus get coexistence with host cells, then host cells allow virus to survive in host with propagation of viruses, reservation of virus genes. Persistent infection is grouped into sub-classifications. One is a chronic infection by hepatitis B and C viruses, and another is a slow infection such as Creutzfeldt-Jakob disease. iii) oncogenic infection; host cells develop cancer via persistent infection after infection of viruses which have the oncogene such as retrovirus. After infection, Viral oncogene is integrated into host chromosomal DNA, resulting in activation of proliferation potency and carcinogenesis of host cell.

death.

Infections by viruses are grouped by the propagation of microorganism into the following categories: i) lytic infection, ii) persistent infection, and iii) oncogenic infection (Figure 2)[1,2]. RNA polymerase from Influenza A virus is involved in lytic infection because of its propagation mechanism in the host cells.

To prevent infectious diseases and to regulate the immune responses, information about the structures of proteins and the interaction between pathogens and host factors are necessary.

Carcinogenic factor, Tipα, from *H. pylori*

H. pylori is a gram-negative pathogenic bacterium that infects gastric epithelial cells in approximately 50% of the world population[3]. *H. pylori* infection causes inflammation in the microenvironment through induction of proinflammatory cytokines, such as TNF-α, interleukin (IL)-1, IL-6, and IL-8, and various chemokines, resulting in chronic gastritis, gastric ulcers, duodenal ulcers, and sometimes cancer[4]. In 1994, the International Agency for Research on Cancer classified *H. pylori* as the definitive carcinogen for humans (IARC Working Group)[5]. *H. pylori* expresses various virulence factors, including immunodominant cytotoxin-associated antigen (CagA), vacuolating cytotoxin (VacA), and urease, all of which have been extensively studied, and positivity for the presence of a cag pathogenicity island (cagPAI) has been strongly associated with the development of gastric ulcers and cancer[6-9]. On the other hand, studies of the mechanisms underlying

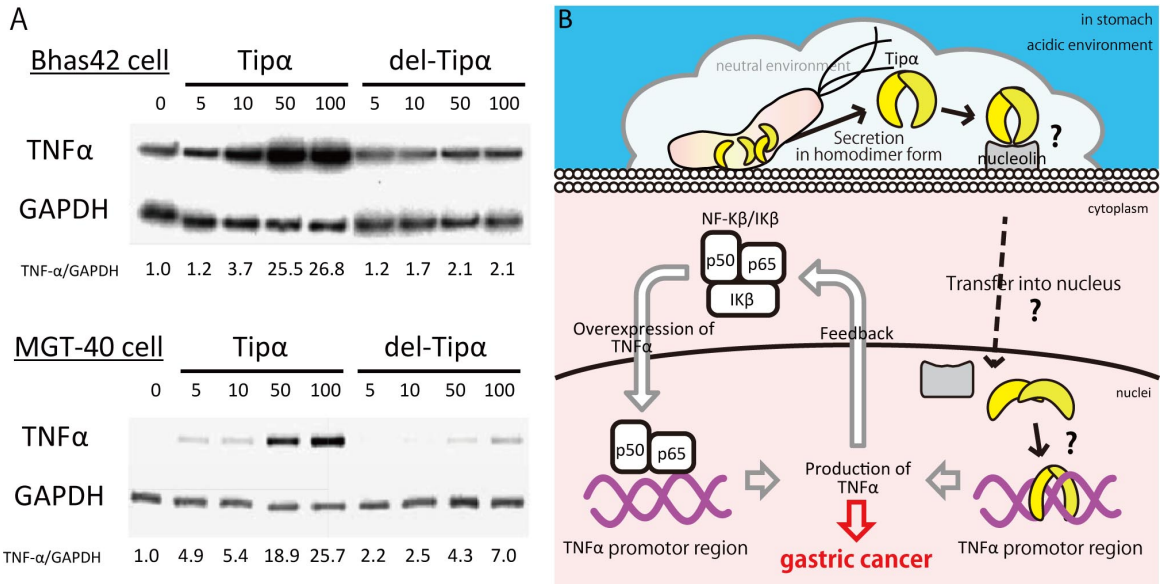

Figure 3 Production of TNF-α induced by Tipα. A) TNF-α production induced by Tipα, not del-Tipα, in Bhas42 cell (upper) and in MGT-40 cell (lower) [10]. B) A probable mechanism of TNF-α production and gastric cancer developing.

the development of stomach cancer in humans also suggest the necessity for additional virulence factors[11,12]. Using TNF-α deficient mice, Suganuma et al. previously demonstrated that TNF-α plays an essential role in tumor promotion[13,14]. In that context, they searched the genome of *H. pylori* strain 26695 for the presence of new genes involved in the induction of TNF-α gene expression in gastric epithelial cells and identified a new gene encoding Tipα, which was named by Suganuma et. al.[15].

The Tipα gene is situated in a region outside the cagPAI and present within the genomes of all *H. pylori* strains examined till date. Moreover, the encoded protein has a unique primary structure and no obvious homologue in any other species as well as bears no similarity to any other *H. pylori* virulence factors. Tipα protein is secreted by *H. pylori* and strongly induces expression of TNF-α (Figure 3A) and various chemokines through activation of NF-κB in gastric epithelial cells[15-17]. Other biochemical features of Tipα include the following: i) it is secreted from the cells as a homodimer in a manner independent of the Type VI secretion system; ii) it activates NF-κB independent of cagPAI; iii) because it is translocated from cell surface to nuclei in the gastric cancer cells; iv) it shows in vitro DNA binding activity, as determined using Biacore; and v) it is a highly immunogenic *H. pylori* protein[10,15,18]. It is noteworthy that cultured *H. pylori* isolated from gastric cancer patients secretes greater amounts of Tipα into the culture medium in comparison with that isolated from patients with chronic gastritis, which suggests that Tipα is involved in gastric carcinogenesis in humans infected with *H. pylori*[10]. In line with this idea, Tipα induces in vitro transformation of Bhas 42 (vH-ras transfected BALB/3T3) cells[15]. To understand how Tipα induces the gastric deseases

```
Tipα      1   MLQACTCPNT  SQRNSFLQDV  PYWMLQNRSE  YITQGVDSSH
                                      N-terminal flexible region
delTipα   1   M------PNT  SQRNSFLQDV  PYWMLQNRSE  YITQGVDSSH
                                      short α          β1

Tipα     41   IVDGKKTEEI  EKIATKRATI  RVAQNIVHKL  KEAYLSKTNR
delTipα  41   IVDGKKTEEI  EKIATKRATI  RVAQNIVHKL  KEAYLSKTNR
                                      α1

Tipα     81   IKQKITNEMF  IQMTQPIYDS  LMNVDRLGIY  INPNNEEVFA
delTipα  81   IKQKITNEMF  IQMTQPIYDS  LMNVDRLGIY  INPNNEEVFA
                         α2                β2          β3

Tipα    121   LVRARGFDKD  ALSEGLHKMS  LDNQAVSILV  AKVEEIFKDS
delTipα 121   LVRARGFDKD  ALSEGLHKMS  LDNQAVSILV  AKVEEIFKDS
               β3         α3                  α4

Tipα    161   VNYGDVKVPI  AM
delTipα 161   VNYGDVKVPI  AM
```

Figure 4 Primary structures of Tipα and del-Tipα. The secondary structures are shown in red (α helix) and yellow (β sheet). The N-terminal flexible region is shown in blue. The N-terminal and C-terminal regions not visible on the electron density map are shown in grey.

from the point of view of structural analysis, we have been working on an X-ray crystallographic analysis of Tipα structure. However, so far, we have been unable to grow crystals of Tipα because of the tendency of the molecule to aggregate. To overcome this problem, we instead crystallized a deletion mutant of Tipα (del-Tipα), which lacks the N-terminal six amino acid residues (LQACTC), including two cysteines (Cys5 and Cys7), that form disulfide bonds (Figure 4). Here, we show the crystal structure of del-Tipα and discuss the conformational change of Tipα in Chapter I.

Propagation mechanism of Influenza A virus

Seasonal influenza virus causes respiratory inflammation, high fever, head and muscle aches, and fatigue. In the pandemic of 1918, the influenza virus (known as the Spanish influenza) also caused severe pneumonia, affecting 50 million victims[19]. Following this pandemic, humans have dealt with the following three influenza pandemics: Asian influenza (H2N2) in 1957, Hong Kong influenza (H3N2) in 1968, and H1N1 influenza in 2009.

The influenza A virus belongs to Orthomyxoviridae and contains eight viral ribonucleopotein (vRNP) complexes, which are composed of viral RNA (vRNA), vRNA-dependent RNA polymerase, and nucleoprotein (NP). vRNP complexes are the basic unit for transcription and replication[20]. vRNA is a single stranded negative chain associated with the RNA polymerase and NPs. The RNA polymerase is a heterotrimer composed of the three subunits, i.e., polymerase acidic protein (PA), polymerase basic protein 1 (PB1), and polymerase basic protein 2 (PB2). This heterotrimeric RNA

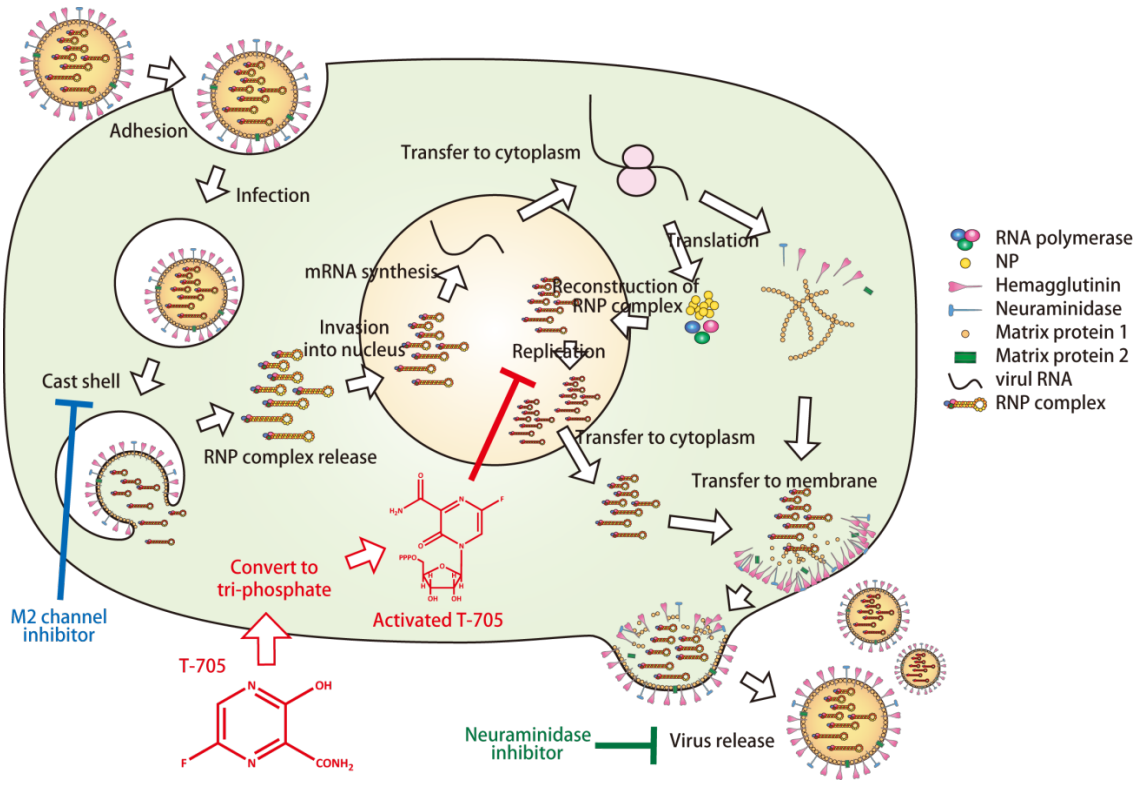

Figure 5 Scheme of influenza virus proliferation from adhesion to release

polymerase undergoes transcription from a negative to a positive vRNA and further, the replication of negative vRNA via the replication of a complementary DNA (Figure 5).

In the transcription reaction, called the cap-snatching mechanism, in the first step, PB2 captures the cap structure of the host 5′-capped mRNA, such as 7-methyl-guanosine-5′-triphosphate (m^7GTP). In the second step, a captured host mRNA is cleaved with 10–13 nucleotides by the endonuclease activity of the PA subunit. Finally, the PB1 subunit plays a central role in the elongation of positive vRNA using the cleaved oligonucleotide as a primer[21].

The middle domain of the PB2 subunit plays a key role in cap binding. Furthermore, PB2 displays a bipartite nuclear localization signal (NLS) in the C-terminal domain and is transported to the nucleus[22]. In addition, residues 627 and 701 in the C-terminal domain of PB2 have been identified as important factors of host range and pathogenicity[23-25]. The crystal structures of the C-terminal domain of PB2 were reported by Kuzuhara et al. and other groups[26,27]; The former structure was the first deposited structure of the PB2 C-terminal domain containing the pathogenicity determinant lysine residue at position 627 in the Protein Data Bank (Apr 21, 2008, 3CW4) and the RNA binding ability of this domain was enhanced by the E627K mutation[26].

Here, we show the crystal structure of the PB2 middle domain (H1N1) complexed with

or without m^{7}GTP, which is a trigger for the cap-snatching mechanism described in Chapter II.

ADP-ribosylation of actin by Ia from *C. perfringens*

Mono- and poly-ADP-ribosylation are ubiquitous and important post-translational modifications in which one or more ADP-ribosyl moieties from NAD$^+$ are added to the target protein in a reaction catalyzed by an ADP-ribosyl transferase (ART)[28] (Figure 6). Mono-ADP-ribosylation was originally identified as the pathogenic mechanism of certain bacterial toxins[29], which were classified into several types on the basis of their respective targets. As type I, *cholera* toxin[30,31], *pertussis* toxin[32], and *Escherichia coli* heat-labile enterotoxin[33] target heteromeric GTP-binding protein, cysteine or arginine. As type II, *diphtheria* toxin[34] and *Pseudomonas* exotoxin A modify elongation factor 2 diphthamide. As type III, *C. botulinum* C3 exotoxin ADP-ribosylates the small GTP-binding protein asparagine[35]. As type IV, *C. botulinum* C2[36] and *C. perfringens* Ia[37] ADP-ribosylate actin arginine. Recently, an atypical ADP-ribosylating toxin was discovered;*Photorhabdus luminescens* TccC3 modifies actin threonine 148[38]. *C. botulinum* C2 toxin was the first reported actin-specific ART, and *C. perfringens* Ia was later shown to have striking similarities in both its enzymatic component (C2I or Ia) and binding/translocation component (C2II or Ib). Thus, both C2I and Ia ADP-ribosylate G-actin Arg177, which leads to cytoskeletal disorganization and cell death[39,40]. Furthermore, Ia and C2I recognize subtle differences in the actin molecule; consequently, Ia modifies both α-actin and β-actin,

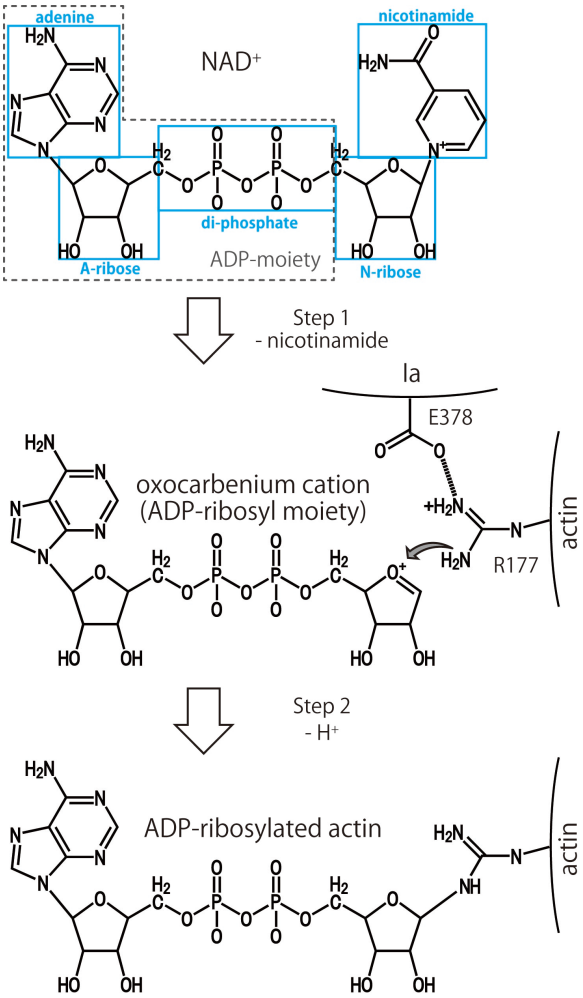

Figure 4 Catalytic mechanism of ADP-ribosylation reaction. Step 1: Cleavage of nicotinamide moiety and production of oxocarbenium cation. Step 2: deprotonation of Arg177 of actin and making bond between NC1 of N-ribose and guanidyl nitrogen of Arg177.

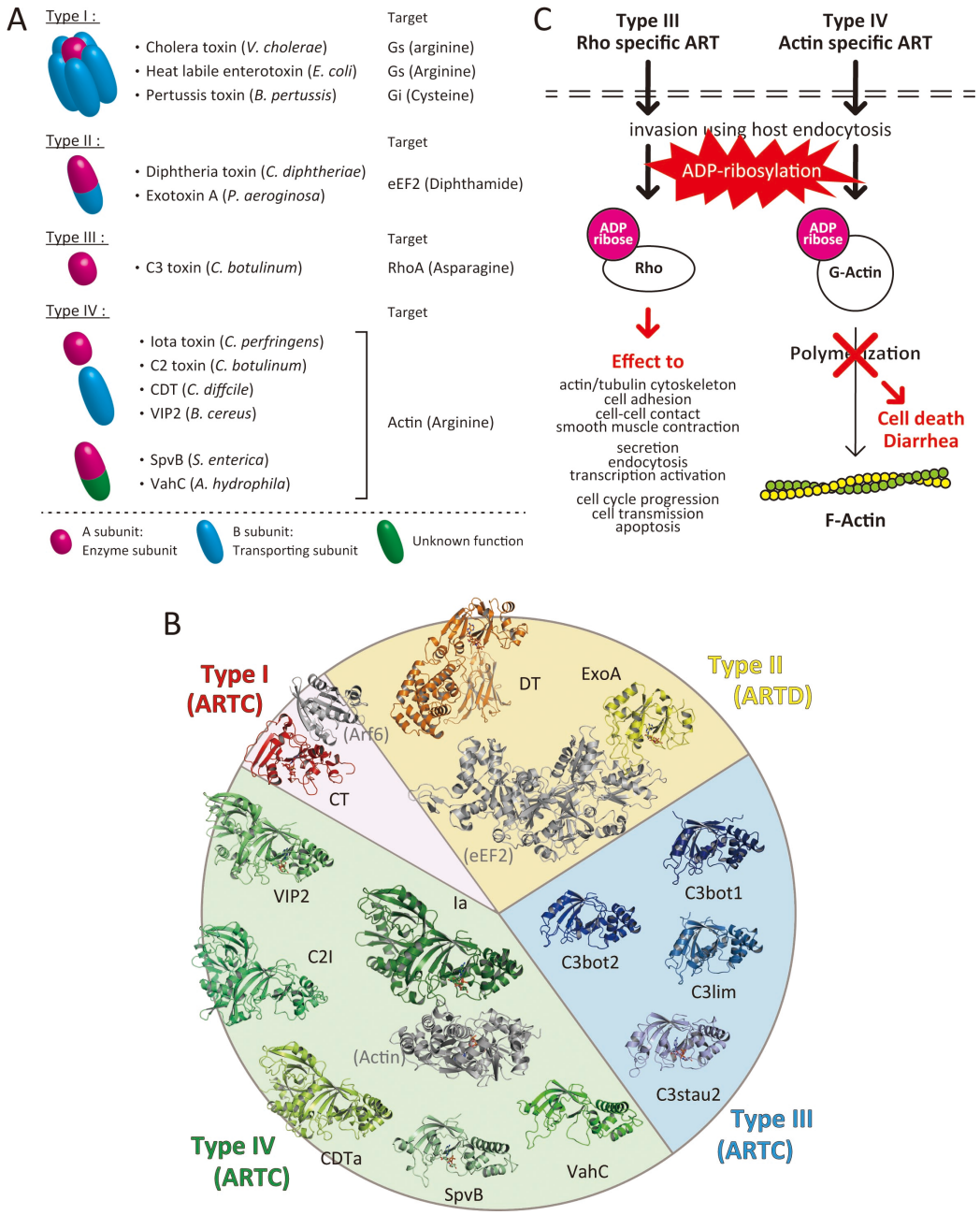

Figure 7 A) Classification of ARTs based on their target specificity. ADP-ribosyltransferase subunit (A subunit), membrane transporting subunit (B subunit) and a component with unknown function are in magenta, blue and green, respectively. B) Structures of ARTs and its NAD binding of each type. Structures of Ia (with actin), C2I, VIP2, CDTa, SpvB, VahC, C3 and CT (with ARF6) are shown, which are classified as ARTCs. The structures of DT and ExoA (with eEF2) are shown, which are classified as ARTDs. There is strong structural similarity in all ART domains with NAD^+ binding. The overall structures of type I, II, III and IV are depicted in red, yellow, blue and green, respectively. Binding proteins are depicted in gray. Accession number in PDB of shown structures are; NAD^+-CT-Arf6 (2A5F), NAD^+-DT (1TOX), NAD^+-ExoA-eEF2 (2ZIT), C3bot1 (1UZI), C3bot2 (1R45), C3lim (3BW8), NAD^+-C3stau2 (1OJZ), NAD^+-Ia-actin (4T03), NAD^+-VIP2 (1QS2), CDTa (2WN4), C2I (2J3X), NAD^+-SpvB (2GWL), and VahC (4FML). C) Effect of ADP-ribosylation by Type III and Type IV ADPRTs.

whereas C2I only modifies ß-actin. The structures of catalytic components or domains from various ARTs (VIP2[41], Ia[42], C2I[43], and CDTa[44] as a two-component toxin/SpvB[45] as single-component toxin) have been determined with and without NAD^+ (Figure 7). In the usual two-component toxin, the catalytic component has two similar domains, which are the C-domain with ADP-ribosyltransferase activity and N-domain with membrane-binding and translocation activity. In catalytic C-domains, they show a strong electrostatic potential similarity[42]. The C-terminal domain shares a conserved ß-sandwich core structure consisting of eight ß-strands. Around the ß-sandwich core, two helices and a loop form the NAD^+-binding site. Not only in type IV but also in type III toxins, the similar structure of the catalytic domain was maintained but the modified target and residue are different (C3bot[46,47], C3stau[48], and C3lim[49]). These structural and biochemical studies of ARTs have provided us with detailed structural information about NAD^+-binding. A particularly important point is that the NMN portion is highly folded into a strained conformation within all ARTs[42,50].

As described above, several single structures of mono-ARTs have been revealed. On the other hand, several mono-ART structures complexed with other proteins have been revealed. However, there are only two complex structures with substrate protein; one is Exotoxin A (ExoA, in Type II) from *Pseusomonas aeruginosa* in complex with elongation factor 2 (eEF2) and intact NAD^+[51]; the other is in Type IV, *C. perfringens* Ia complexed with actin and a NAD^+ analog, which was revealed by Tsuge et al.[52]. However, it was not sufficient to clarify the ADP-ribosylation mechanism from only two complex structures.

In Chapter III, we revealed the following complex structures: the complex structure of Ia as ADPRTase, NAD^+ as a substrate, and actin as a substrate protein; the complex structure of Ia and ARP-ribosylated actin. From these structures, we have refined and confirmed the ADP-ribosylation mechanism suggested by Tsuge et al.[52].

Chapter 1:

Conformational change of carcinogenic factor TNF-α inducing protein from *Helicobacter pylori*

I.1 Introduction

Stomach cancer is strongly associated with infection by *Helicobacter pylori*. In 2005, Suganuma et al. identified a new *H. pylori* gene encoding a TNF-α inducing protein (Tipα) that acts as a carcinogenic factor. Tipα is secreted from *H. pylori* as a homodimer whose subunits are linked by disulfide bonds. They also characterized a Tipα deletion mutant (del-Tipα) that lacks the N-terminal six amino acid residues (^{2}LQACTC^{7}), including two cysteines (Cys5 and Cys7) that form two disulfide bonds between subunits, and Nu-PAGE analysis showed del-Tipα to be a monomer in both the absence and presence of dithiothreitol[15]. The biological activity of del-Tipα is 10–50 times weaker than that of Tipα, as reflected by its diminished binding and uptake by gastric epithelial cells and its diminished ability to induce TNF-α gene expression[10,15]. Here we report that del-Tipα has a novel elongated structure containing a 40 Å-long α helix, and forms a heart-shaped homodimer via non-covalent bonds. Moreover, their circular dichroism spectra strongly suggest that the structures of the del-Tipα and Tipα homodimers are very similar.

Now, several structures of truncated Tipα mutant are revealed. Therefore, we classified them into two groups and named. That is, one is defined as "Tipα" which is wild type and truncated mutant including two cysteines (Cys5 and Cys7) and another is defined as "del-Tipα" which is a truncated mutant without two cysteines. The structures of del-Tipα are reported by us, Tosi et al.[53], and Jang et al.[54] and that of Tipα is reported by Gao et al.[55]. All of them include dimer form in crystal and they showed two conformations; open and closed conformation, which are called "open jaw" and "closed jaw", respectively. According to their crystallization conditions, it seems that the conformational change occurs depending on pH of environment; closed jaw and open jaw is seen at slightly basic and acidic condition, respectively. In Tipα, by improving crystallization condition, at last

we obtained the crystals at pH 5.0 and its 2.9 Å data set. We keep modeling and refinement using this data set, it seems that Tipα in pH 5.0 is in open jaw conformation as well as Gao et al.[55] and as well as del-Tipα. However conformation of Tipα in basic condition has not been revealed. We analyzed dimer conformation using X-ray small angle scattering analysis, according to this result, both Tipα and del-Tipα formed open jaw conformation at pH 4.0 and closed jaw at pH 8.0 (Ikeguchi et al. unpublished data). These results suggest that Tipα dimer forms open jaw at acidic condition and closed jaw at slightly basic condition as well as del-Tipα. However, it is not clear when and how to induce TNF-α by Tipα. To answer this question, we prepare Tipα mutant to make fixed open form dimer or fixed closed form dimer. We will reveal which open or closed form dimer induces TNF-α using fixed form dimers.

This unique mode of Tipα dimer formation provides important insight into protein-protein interactions and into the mechanism underlying the carcinogenicity of *H. pylori* infection.

I.2 Materials and Methods

I.2.1 Sample preparation and crystallization of Tipα

del-Tipα gene was amplified by PCR using genomic DNA from *H. pylori* strain 26695 with primers AGAGCATATGCCAAACACTTCACAAAGGAA and TCTCGGATCCTACATGGCTATAGGGACTTT, and cloned into pET28(a)+ vector[15]. Then, Tipα and del-Tipα genes in pET28(a)+ vector were expressed in *Escherichia coli BL21* following addition of 0.4 mM isopropyl-β-D-thiogalactopyranoside (IPTG) to the culture for 5 hours at 37 °C, as described previously[15]. The cells were then collected by centrifugation, re-suspended in lysis buffer containing 10 mM Tris-HCl (pH 7.4), 0.3 M NaCl and a protease inhibitor cocktail (Complete, EDTA-free, Roche), and disrupted using a French press. Cell lysates containing the His-tagged recombinant del-Tipα and Tipα proteins were then loaded onto a Ni^{2+} chelating agarose column (Protino Ni-TED column, Marcherey-Nagel). After cleaving the thrombin cleavage site of recombinant protein using a Thrombin kit (Novagen), the His-tagged fragments were separated from protein by the Ni^{2+} chelating agarose column. The purity of del-Tipα and Tipα proteins was >98% on Nu-PAGE (Invitrogen).

I.2.2 Data collection and model building

Crystals of del-Tipα were grown for 1-2 weeks at 4 °C using the hanging drop vapor diffusion method with equal volumes of protein solution (10–15 mg/ml) and mother solution comprised 10% PEG6,000, 5% MPD, 0.1 M HEPES (pH 7.5) or 25%

tertiary-butanol 0.1 M Tris-HCl (pH 8.5). Crystals in tertiary-butanol grew more rapidly than those in PEG6,000; however, data collection was carried using PEG6,000 crystals because of their quality and milder treatment. X-ray data were collected at 100 K in cryo-protectant buffer consisting of 30% glycerol in mother solution. Heavy metal derivatives were prepared by soaking the crystals for various periods in solutions containing various concentrations of platinum (K_2PtCl_4). The images were processed using HKL2000[56] and SCALA[57]. The crystals were highly non-isomorphous, so we examined several combinations of native and heavy atom derivatives, and then calculated the phases. The phases were obtained using SOLVE and RESOLVE[58], and space group was found to be $P3_221$. Initial phases were calculated at 3.2 Å using data from the native crystal and two platinum atom derivatives, which were collected on FR-E and RAXIS VII (RIGAKU). That initial phase was then combined with another phase calculated at 2.47 Å resolution using one native crystal and one platinum derivative, with anomalous dispersion data collected on beamline PF BL-5A at the KEK Photon Factory (Tsukuba, Japan). The data collection and refinement statistics are summarized in Table I-1. The initial model was constructed using XtalView[59]. Iterative model building and refinement using the REFMAC5 module of the CCP4 suite[57] were conducted with 2.47 Å native data. Finally, TLS refinement was carried out to reduce *R*free. The final values of *R*work and *R*free were 22.6% and 28.1%, respectively. The model geometry was determined using PROCHECK[60], and the calculated Ramachandran

Table I-1 Data collection and structure refinement statistics of del-Tipα

	Native	Pt01	Pt02	Pt03 (anomalous data)
Data collection				
Wavelength (Å)	1.00	1.54	1.54	1.07
Resolution (Å)	50.0 - 2.47	50.0 - 3.4	50.0 - 3.6	50.0 - 3.68
Number of unique reflections	7,160	3,060	2,567	10,172
Completeness (%)	98.3 (100.0)	99.7 (100.0)	99.6 (100.0)	95.0 (94.8)
*R*sym*	0.061 (0.133)	0.068 (0.390)	0.095 (0.385)	0.057 (0.354)
I/sigma(*I*)	21.3	10.5	10.1	29.8
Redundancy	7.0	5.2	5.1	5.0
MIRAS phasing FOM	0.32			
Refinement				
Resolution (Å)	50.0 - 2.47			
*R*work**	0.226			
*R*free***	0.281			
RMSD bond length (Å)	0.019			
RMSD bond angle (°)	1.844			
B-values	39.4			
Number of residues in outlier region of Ramachandran plot	0			

Values in parentheses are for the last resolution shell. *$R\mathrm{sym} = \Sigma hkl\, \Sigma i |li(hkl) - \langle l(hkl)\rangle| / \Sigma hkl\, \Sigma i |li(hkl)|$, where $li(hkl)$ is the intensity measurement for a reflection hkl, $\langle l(hkl)\rangle$ is the mean intensity for this reflection. **$R\mathrm{work} = \Sigma hkl ||Fobs| - |Fcalc|| / \Sigma hkl |Fobs|$. ***$R$free was calculated with randomly selected reflections (5%).

plot showed 90.2% of residues to be in the most favored region, with no residues in the disallowed region. The model includes 141 amino acids (19–160) and 42 water molecules. The N-terminal 12 amino acids and C-terminal 12 amino acids were not visible in the experimental electron density map. The atomic coordinates and structure factors (code 3GUQ) have been deposited in the Protein Data Bank.

I.2.3 Circular dichroism measurement

CD (circular dichroism) spectra were measured using a J-820 spectropolarimeter (Jasco) at 25 °C. The path length of the optical cell was 2 mm for the far-UV CD measurements and 10 mm for the near UV CD measurement. The final protein concentrations used for the far-UV spectra were 13 and 19 µg/ml for Tipα and del-Tipα, respectively; for the near-UV spectra, the concentrations were 128 and 186 µg/ml for Tipα and del-Tipα, respectively

I.3 Results and Discussions

I.3.1 Overall structure of del-Tipα

The crystal structure of del-Tipα was determined using MIRAS (multiple isomorphous replacement with anomalous scattering). The del-Tipα monomer has an elongated structure with a long axis of about 50 Å and a novel α1-ß1–α2–α3–ß2–ß3–α4–α5 topology (Figure I-1). The key feature of del-Tipα is the 40 Å-long α helix (α2) that extends from the bottom to the top part of the molecule (Figure I-1A). The bottom part of the molecule is made up of a portion helix α2 enveloped by a three-stranded, anti-parallel ßsheet, while the top part is made up of a 4-helix bundle comprised of the remainder of α2 and α3, α4 and α5. The 4-helix bundle appears to be stabilized through hydrophobic interaction among the four helices; the interacting residues were Ile66, Val67, Leu70 and Ala73 of α1; Phe90, Met93 and Ile97 of α2; Leu132, Leu136 and Met139 on α3; and Ala145, Ile148, Leu149, Val153 and Ile156 of α4. By contrast, a large number of hydrophilic residues are present on the surfaces of the four-helix bundle. In addition, a unique flexible N-terminal region, extending from Asp19 to Ile32, makes up a short helix (α1, ^{21}PYWML^{25}), part of which is important for the dimerization of del-Tipα, which will be discussed later. A search of the sequence database revealed no obvious sequence homology between Tipα and any known proteins; consequently, 3D modeling programs like Geno3D[61] could not be used for construction of 3D models. A structural similarity search using the MATRAS and DALI web servers[62] revealed a few structures that closely resembled del-Tipα. MATRAS indicated that there is the structural homology between the bottom part of del-Tipα (part of α1 and ß1, ß2 and ß3) and two proteins: acetamidase (2ii1: Zscore = 10.2)

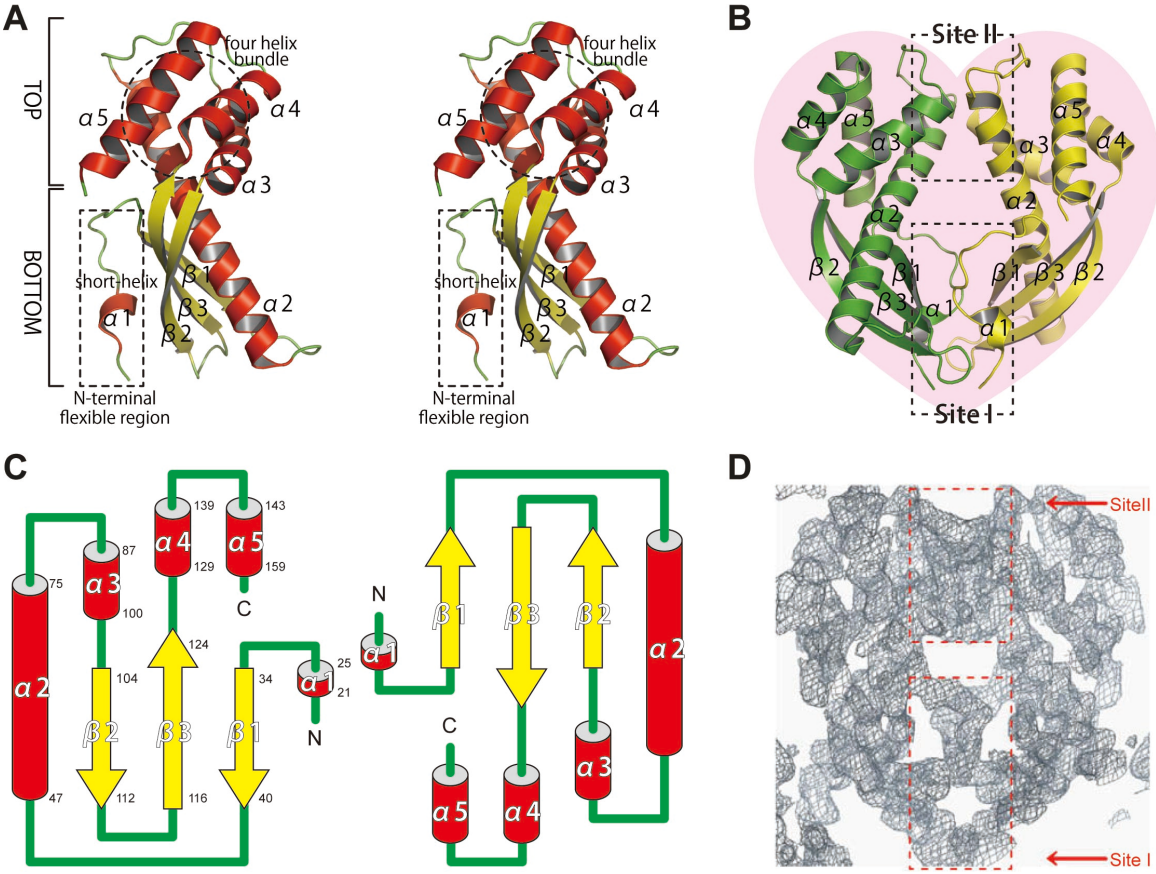

Figure I-1 Overall structure of del-Tipα. A) Stereochemical structure of del-Tipα monomer. The α helices and β sheets are shown in red and yellow, respectively. Note the elongated shape of the monomer. The N-terminal flexible region with short α helix (α1) is boxed. B) Tertiary structure of the heart-shaped del-Tipα dimer. Molecules A (green) and B (yellow) correlate with two-fold crystallographic symmetry. C) Topology diagram of the del-Tipa dimer. The flexible N-terminal regions are in close proximity. D) Experimental electron density map determined by multiple isomorphous replacement contoured at 1 sigma. The map was calculated at 2.47 Å resolution.

and dodecin[63] (2vx9: Z-score = 9.9). Similarly, the DALI web server also found homology between del-Tipα and dodecin (Z-score = 4.9). Despite their similar topologies, the length of the αhelix in dodecin is substantially shorter than α1 in del-Tipα. Moreover, dodecin is a flavoprotein that binds FAD, but the amino acid residues in the FAD binding site of dodecin are not conserved in del-Tipα. In an earlier report, we discussed the structural similarity between Tipα and PBP (penicillin-binding protein), based on the sequence similarity of the conserved binding motif[64]. However, the findings of the present study show that the fold of Tipα is completely different from that of PBP. Indeed, our findings strongly indicate that, with its long α helix, which appears to serve as a backbone for the molecule, the overall fold of del-Tipα is novel.

I.3.2 Quaternary structure of del-Tipα

The crystallographic asymmetric unit of del-Tipα consists of a monomer (molecule A).

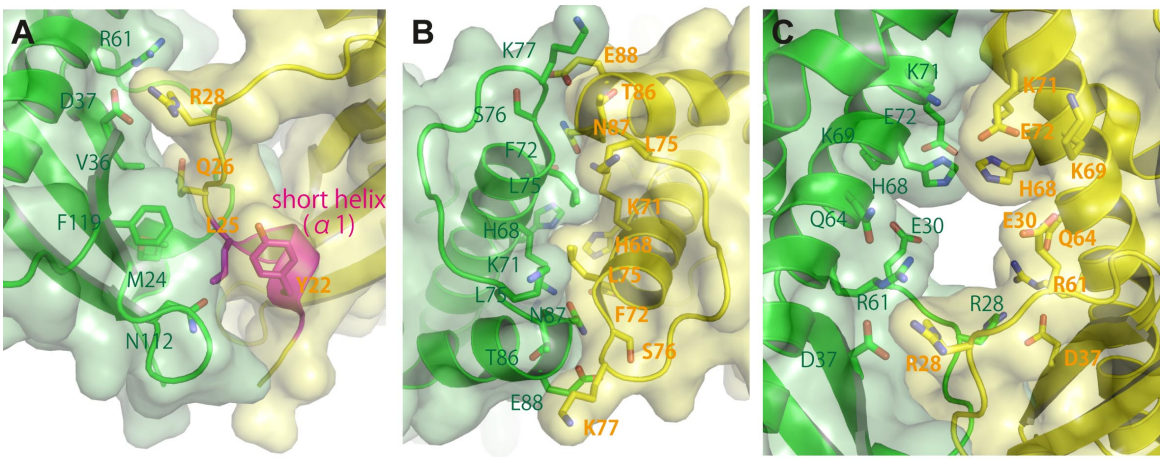

Figure I-2 Close-up view of molecular interaction sites I and II. The locations of sites I (A) and II (B) within the dimer are also shown in Figure I-1B and I-1D. The short helix is colored in magenta. C) Close-up view of the hole in the del-Tipα dimer.

Nonetheless, molecule A can interact with another monomer (molecule B) along a crystallographic two fold axis to form a heart-shaped dimer with a hole at its center (Figure I-1B, C). The two monomers are linked through electrostatic and hydrophobic interactions, which occur at site I in the flexible N-terminal region and at site II (Figure I-1B).

Figure I-1D shows the experimental electron density around His68 from each monomer at site II. At site I, the electron density of the N-terminal 12 amino acids is not visible due to the region's flexibility. The first visible amino acids (Asp19) in the N-terminal portions of molecules A and B are in close proximity. Therefore, it seemed that two cysteines of each molecule interact and make disulfide bridges. This structural feature of del-Tipα suggests that the disulfide bridges on the N-terminal portions of the molecules maintain the dimerization state of Tipα. What is more, the short helices (α1) in the N-terminal flexible regions of the two molecules interact through Tyr22, Leu25, Gln26 and Arg28 of molecule A and Met24, Val36, Asp37 and Phe119 of molecule B (Figure I-2A); and at site II, molecules A and B interact with each other through His68, Lys71, Glu72, Ser76, Asn87 and Glu88 (Figure I-2B). The hole in the center of the del-Tipα dimer has a diameter of about 10 Å and is formed by hydrophilic residues: Arg28 and Glu30 at site I; His68, Lys69, Lys71 and Glu72 at site II; and Arg61 and Gln64 (Figure I-2C). Recently, we found that Tipα bound to DNA oligomers more strongly than del-Tipα and that Mg^{2+} stimulates the binding, as is seen in other known DNA-binding proteins[18].

I.3.3 Structural similarity between Tipα and del-Tipα in solution

Despite extensive crystallization trials, we have not yet obtained diffraction-quality crystals of Tipα. We therefore evaluated the solution structures of Tipα and del-Tipα by

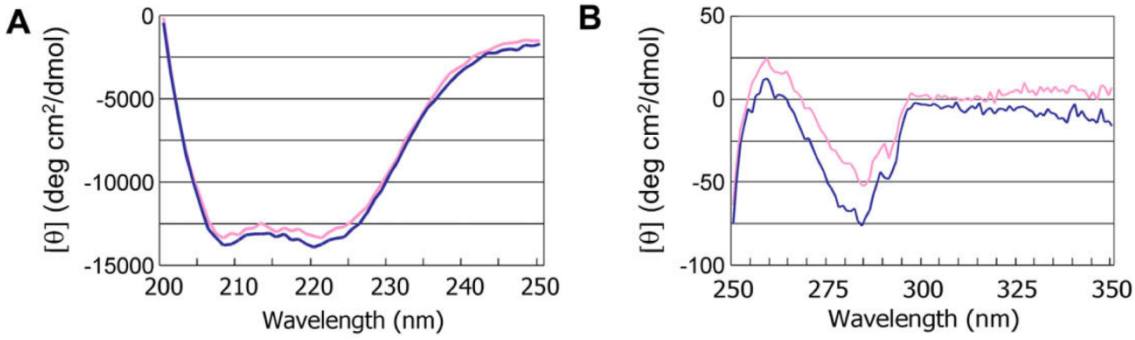

Figure I-3 CD spectra for Tipα (blue) and del-Tipα (pink). A) Far-UV region (200–250 nm). B) Near-UV region (250–350 nm).

comparing their CD spectra. It is well established that the CD spectrum in the near-UV region reflects the three dimensional structure of a protein, while the far-UV region reflects the secondary structure (e.g., α helix and β sheet). We obtained the strongly similar CD spectra in both the near-UV (Figure I-3A) and far-UV (Figure I-3B) regions and the data clearly show that Tipα and del-Tipα have the strongly similar features, which suggests that the solution structures of Tipα and del-Tipαare the same, despite the fact that Tipα contains disulfide bonds and del-Tipα does not. Based on the structural features of Tipα and del-Tipα and the similarity of their CD spectra, we conclude that Tipα has the same elongated structure with a 40 Å-long α helix (α2) as del-Tipα and forms the same heart-like dimer as del-Tipα. However, described above, Tip α has two cysteine residues on N-terminus, which may interact each other closely. This only one difference between Tip α and del-Tip α

Although one Tipα family member, *H. pylori*-membrane protein 1 (HP-MP1), has been reported to be membrane-bound[65], Suganuma et al. found that neither HP-MP1 nor Tipα has a hydrophobic surface to interact with the lipid layer of the membrane. Tipα is secreted from *H. pylori* as a soluble homodimer by certain secretion mechanism, not Type VI secretion system[10,15]. Interestingly, Tipα proteins reach the nucleus, probably aided by specific binding proteins[10]. Once in the nucleus, Tipα induces expression of TNF-α and various chemokine genes through activation of NF-κB, thereby stimulating cell transformation[17]. Thus, the carcinogenic component of Tipα activity is quite different from that of CagA. We therefore speculate that its novel structure may be related to as yet unidentified mechanisms for secretion from *H. pylori* and incorporation mechanism into the nucleus.

I.3.4 Conformational change of Tipα and del-Tipα

Several structures of three kinds of truncated Tipαs (TipαN5; deleted Signal peptide

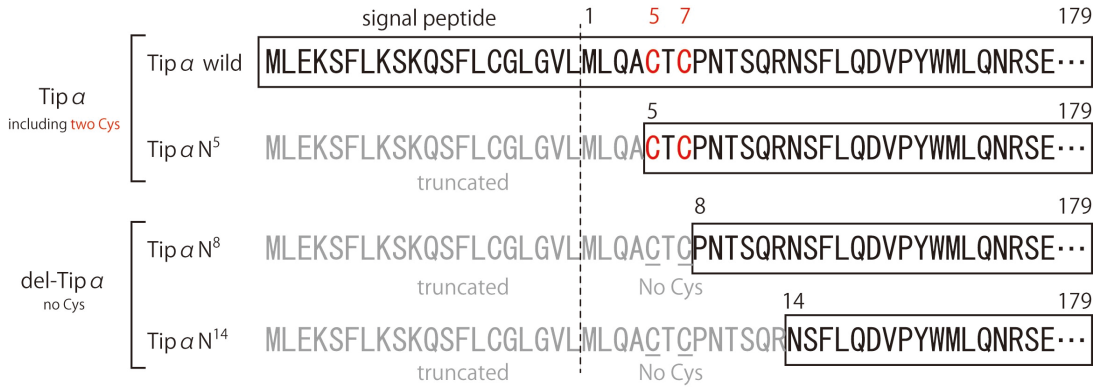

Figure I-4 Classification of truncated mutants of Tipα. Tipα wild and N^5 possess two cysteines Cys5 and Cys7, belonging to Tipα. On the other hand, N^8 and N^{34} do not possess two cysteines, belonging to del-Tipα. Gray characters are truncated region and sequences in the box are expressed and used to crystallization except for wild type.

and 1-4, TipαN8; deleted signal peptide and 1-7 and TipαN14; deleted signal peptide and 1-13) were revealed by four groups including us as described later. Therefore, we call the wild type and TipαN5 including the essential Cys5 and Cys7 residues for TNF-α induction as "Tipα" and we call TipαN8 and TipαN14 with two cysteines deleted as "del-Tipα" (Figure I-4). These structures were grouped into two conformations; 1) closed jaw of del-Tipα reported by us (PDB; 3GUQ), Tosi et al. (2WCR) and Jang et al. (3GIO), 2) open jaw of del-Tipα reported by Tosi et al. (2WCQ), and open jaw of Tipα reported by Gao et al. (3VNC) (Figure I-5). From these structures and their crystallization conditions, dimer took closed jaw structure at slightly basic condition (approximately pH 7 - 8). On the other hand, open jaw structure is revealed from the crystals at acidic condition (approximately pH 3.5) (Figure I-5).

Since protein tended to precipitate easily, we could not obtain the crystals of Tipα. Improving the crystallization condition, finally we also obtained crystals at pH 5.0 and its 2.9 Å data set of Tipα. Although this data set is under refinement, the dimer of Tipα at acidic condition seems to be open jaw conformation as well as Gao et al.[55] and as well as del-Tipα (Figure I-5). This result ensured the fact that conformational change occurs depending on pH. Additionally, preliminary X-ray small angle scattering analysis (Ikeguchi et al. unpublished results) revealed that Tipα dimer forms open jaw at basic condition and closed jaw at acidic condition in solution. It also supported that conformation of dimer depends on pH.

In closed jaw dimer, monomers interacted at sites I and II as described above. There are intermolecular interactions between monomers at Met24 (O)-Leu25N (N) and Leu25 (N)-Gln26 (ND1) in site I (Figure I-6B), and at Lys71 (NZ)-Glu72 (OE1) , Leu75 (O)-Asn87 (N), and Lys77 (N)-Gln88 (OE2) in site II (Figure I-6A). In open jaw dimer, there are interactions at intermolecular Ser15 (O)-Asn27 (N), Leu17 (N)-Leu25 (O),

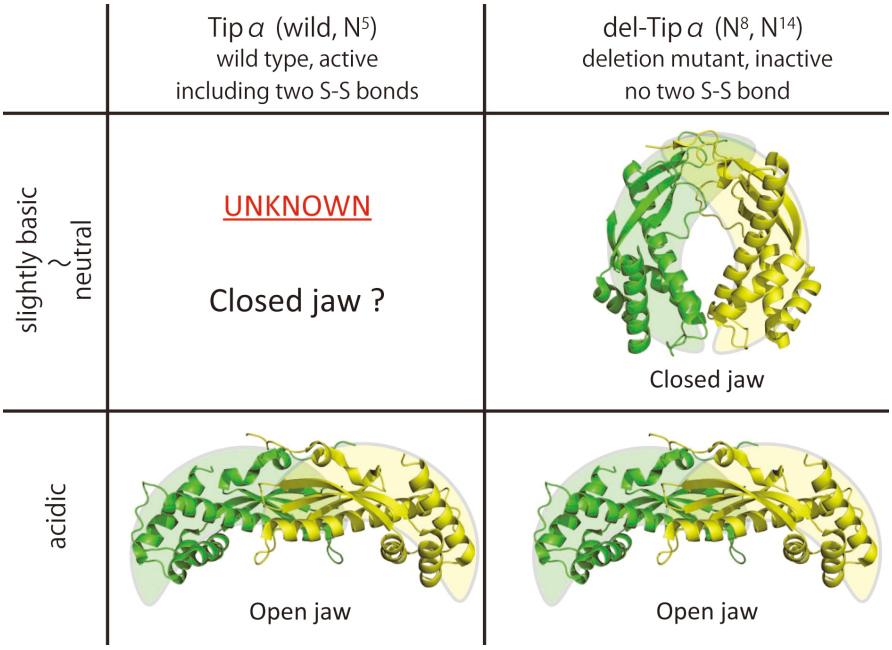

Figure I-5 Dimer conformation of Tipα and del-Tipα. Closed jaw of del-Tipα at neutral condition is revealed by us (PDB; 3GUQ), Tosi et al. (2WCR)[53] and Jang et al. (3GIO)[55]. Open jaw of del-Tipα at acidic condition is revealed by Tosi et al. (2WCQ)[53]. Whereas the structure of Tipα at neutral condition has not been revealed, open jaw of Tipα at acidic condition reported by Gao et al. (3VNC)[54].

His40 (NE2)-Glu127 (OE1), Gln26 (O)-Asn114 (ND2), Arg28 (N)-Asn114 (OD1) and Asp37 (OD1)-Asn115 (ND2) in site I (Figure I-6C) and at intramolecular His68 (NE2)-Glu72 (OD1) and Lys71 (NZ)-Asn87 (OD1) in site II (Figure I-6D, E). Because pKa of histidine side chain is approximately 6.4, there are key features at neutral condition as follows; Site I) There is no intermolecular interaction between His40 (NE2) and others, Glu117 (OE1) and others; Site II) His68 (NE2) and Glu72 (OE1) have a neutral and negative charge, respectively, resulting in the weaker intramolecular interaction between His68 and Glu72. Instead, Glu72 (OE1) interacts with of Lys71 (NZ), which has a positive charge, via intermolecular interaction by ionic bond (Figure I-6). On the other hand, at acidic condition, there are key features as follows; Site I) His40 (NE2) has a positive charge and interacts with Glu117 (OE1), which has a negative charge via intermolecular interaction by ionic bond; Site II) His68 (NE2) has a positive charge and makes intramolecular interaction with Glu72 (OE1), leading the collapse of Lys71 (NZ)-Glu72 (OE1) intermolecular interaction and Lys71 (NZ)-Asp87 (OD1) intramolecular interaction (Figure I-7). It is indicated that the change of His68 charge triggers the change of interaction pair among site II residues (Figure I-7). Additionally, although the structure of N-terminal region including two cysteines has not been observed, we guess that N-terminus including Cys5 and Cys7 needs to play some important roles in dimerization and conformational change at both conditions because at

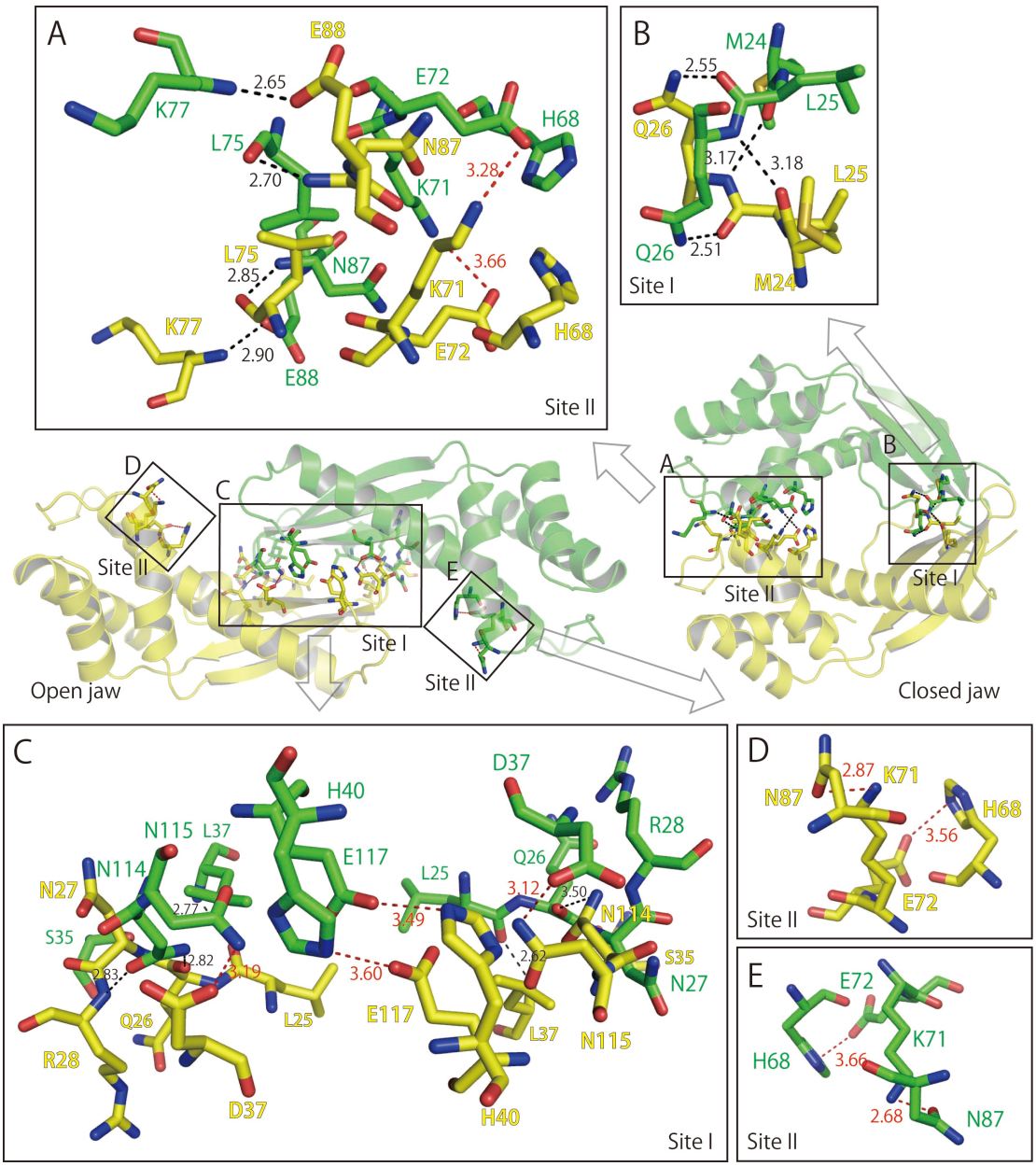

Figure I-6 Interaction between monomers in open and closed jaw, respectively. A) At site II in closed jaw. B) At site I in closed jaw. C) At site I in open jaw. D) and E) At site II in open jaw. Monomers are colored in green and yellow, respectively. Interactions between main and side chain and between main and main chain are depicted black dashed line, and interactions between side and side chain are depicted red dashed line.

least one disulfide bond is essential for TNF-α inducing[10].

H. pylori lives in a stomach, which is a strong acidic environment, and survives by neutralizing its circumstance with ammonia produced by own urease. It is suggested that conformational change of Tipα dimer occurs in each acidic or neutralized condition. However, it is unclear when and how to induce TNF-α by Tipα. Suganuma et al. found that at least one of the cysteine residues is required for potent induction of biological activity at neutral pH[10]. This suggests that formation of a stable Tipα dimer with a

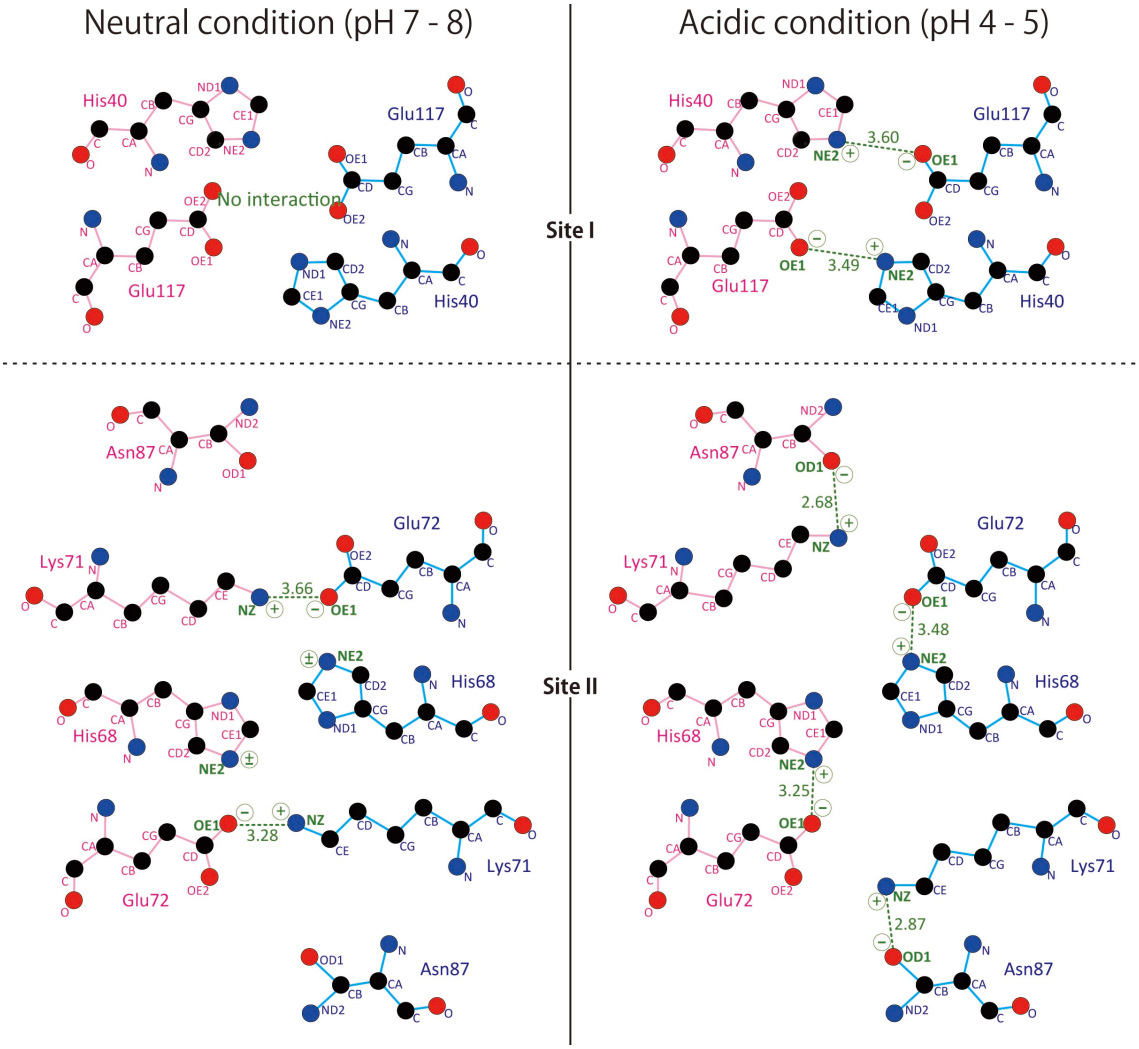

Figure I-7 Interaction between monomers of site I and II at neutral and acidic condition. Monomers are colored in green and yellow, respectively. Key atoms, interactions and charges are depicted and labeled in red.

disulfide bonds is required for full activity[10]. In acidic condition, sulfate atoms of cysteine residues might be protonated and could not link each other, causing unstable dimer. On the other hand, they might be deprotonated and link the disulfide bonds, causing stable dimer with site II interaction in neutralized condition. That is, it is indicated that TNF-α might be induced by closed jaw (or conformational change from open to closed jaw) of Tipα stabilized by two disulfide bonds in neutral condition. However, we cannot state about this, because there is no structural information of DNA binding. To answer this question, we prepare cysteine-mutant of Tipα to make fixed open form dimer or fixed closed form dimer. We will reveal which open or closed dimer induces TNF-α using this mutant.

Chapter II:

Initial action of cap snatching mechanism of Influenza RNA polymerase

II.1 Introduction

Influenza pandemics with human-to-human transmission of the virus are of great public concern. It is now recognized that a number of factors are necessary for human transmission and virulence, including several key mutations within the PB2 subunit of RNA-dependent RNA polymerase. The cap binding site locates in the middle domain of PB2. The crystal structures of this domain from three strains were reported; human H1N1 PB2 middle domain without 7-methyl-guanosine-5'-triphosphate (m^7GTP)[66], human H3N2 PB2 middle domain with m^7GTP[67,68] and human H5N1 PB2 middle domain with m^7GTP[68], thus the middle domain is considered to be novel target for structure-based drug design. However, the structure of PB2 middle domain from H1N1 complexed with m^7GTP has not been reported.

We purified the protein of human H1N1 PB2 middle domain under the high salt condition and also obtained the crystals. As the crystals were not good quality, we collected the data set with considerable difficulty. Although, using this crystal, we obtained the crystal of PB2 middle domain with m^7GTP by a soaking method, the electron density of m^7GTP was not observed by the preliminary structural analysis. The surface of PB2 middle domain molecule tends to hydrophobic, thus the protein would be solubilized in the presence of high salt. So, we prepared PB2 middle domain with two mutations (P453H and I471T), which are far from and may not affect to cap binding site, resulting in increasing the solubility of the protein.

Here we report the crystal structure of the middle domain of H1N1 PB2 with or without m^7GTP at 1.9 Å and 2.0 Å resolution, respectively, which has two mutations, proline to histidine at 453 and isoleucine to threonine at 471 (P453H, I471T), to increase electrostatic potential and solubility. Here we report the m^7GTP has different conformation from the reported structure. 7-Methyl-guanine is fixed in the pocket, but

particularly significant change is seen in ribose and triphosphate region: the buried 7-methyl-guanine indeed binds in the pocket forming by His357, Phe404, Glu361 and Lys376 but the triphosphate continues directly to the outer domain. The presented conformation of m^7GTP may be a clue for the anti-influenza drug-design.

II.2 Materials and Methods

II.2.1 Sample preparation and crystallization of PB2 middle domain

The *pb2* gene (RIKEN) was inferred from the amino acid sequence of influenza virus H1N1 (A/Puerto Rico/8/1934). We used DNA encoding residues 318-483 subcloned into pET15b vector between the NdeI and BamHI sites. The PB2 middle domain (318-483) was then expressed with an N-terminal histidine-tag and a thrombin cleavage site in *E. coli* BL21-CoDonPlus-RIL cells (Agilent Technologies) growing in LB medium. The protein was purified by affinity capture on a Ni-IDA 2000 column (MACHEREY - NAGEL). After elution with imidazole, the protein was cleaved with thrombin and loaded onto an Uno S column (Bio-Rad) and eluted with a salt gradient (0.5 M - 1 M NaCl). The eluted PB2 middle domain was not dissolved well under 500 mM NaCl concentration. To obtain more soluble domain, we introduced two mutations on the surface of this domain: P453H and I471T. The final protein was then concentrated to 10 mg/ml in 50 mM Tris-HCl (pH 8.0), 200 mM NaCl and 2 mM DTT and stored at -80 °C. At N-terminal and C-terminal, there are additional four residues each, ^{314}GSHM^{317} and ^{481}GSGC^{484}, respectively.

Crystals were grown using the hanging-drop vapor diffusion method. The protein solution was mixed with an equal volume of well solution (1.2 M NaCl and 2.5% (v/v) ethanol) and incubated at 4 °C.

II.2.2 Data collection and model building

Crystals were picked up using a nylon loop. They were then dipped in mother liquor containing 20% (v/v) ethyleneglycol as a cryoprotectant and plunged into a nitrogen-gas stream at 100 K. The data were collected using an X-ray wavelength of 1.54 Å using Micro7HFM RAXISVII. The diffraction images were indexed, integrated and scaled using HKL2000 program[56]. The crystal space group was determined to be R32. Initial phase was obtained by molecular replacement (phaser) using H3N2 cap-binding domain structure 2VQZ[69]. The structure was refined using phenix.refine restraint refinement and TLS refinement[70]. Model building and manual refinement was done by Coot[71]. Comparison of the structures was done using PyMOL[72]. Data statistics such as *R*merge, *R*meas, *R*pim and $CC_{1/2}$ were obtained by Xtriage of phenix[73].

The missing residues of electron density are ^{314}G (N-terminal) and ^{481}GSGC^{484} (C-terminal) in native and ^{314}GSHMRS^{319} (N-terminal) and ^{481}GSGC^{484} (C-terminal) in m^{7}GTP, respectively.

II.3 Results

II.3.1 Properties of the middle domain of PB2 (H1N1)

We initially purified His-tagged PB2 middle domain using a nickel chelate column[67]. However, the fraction eluted with 200 mM NaCl was not stable, and aggregation of the protein could be seen. We therefore modified the protocol to elute the protein with 500 mM NaCl and found that the PB2 (H1N1) middle domain was stable under these high salt conditions. We could obtain the crystals and data sets, but both the qualities of crystals and data were not good for the further handling (Figure II-1). Next we considered to change the surface electrostatic potential and to increase the middle domain solubility by mutations. Two mutations (P453H and I471T) were introduced because these positions are surface of the protein and far from cap-binding site.

These mutations increased the solubility so that the final protein was stable in 50 mM Tris-HCl (pH 8.0), 200 mM NaCl. Crystals appeared in two or three days and reached to ~0.3mm size (Figure II-1). We collected the native data sets at 2.00 Å resolution with in-house X-ray generator and detector (Table II-1). We also collected the data set of m^{7}GTP soaked crystal in 0.5 mM m^{7}GTP for 2.5 hours, at 1.93 Å (Table II-1). The upper limit resolutions of these data were carefully chosen including the recent discussion of $CC_{1/2}$[74]. The final *R*work and *R*free was 18.6% (22.1%) and 18.3% (22.8%), respectively (Table II-1).

II.3.2 Structure of the H1N1 PB2 middle domain

There was one molecule in an asymmetric unit (Figure II-2). This crystal contains large solvent content (76%), and two mutations P453H and I471T located on the solvent accessible surface in the crystal packing. The similar minimal cap binding domain structure has been revealed before (PDB ID: 2VQZ)[67]. The overall fold was the same as reported as the reported structure: a four helix bundle (α1 ~ α4) was wrapped by three parts of β-sheet ((1) β1, β2, β5, β6 and β7, (2) β8 ～ β12 and (3) β3 ~ β4). However, compared with the reported structure of PB2 middle domain, in native, one large structural change could be seen: N-terminal region formed one additional α-helix which consists of ^{315}SHMRISS^{321} (Figure II-2 and Figure II-3).

The first three residues (^{315}SHM^{317}) are additional residues derived from pET15b vector.

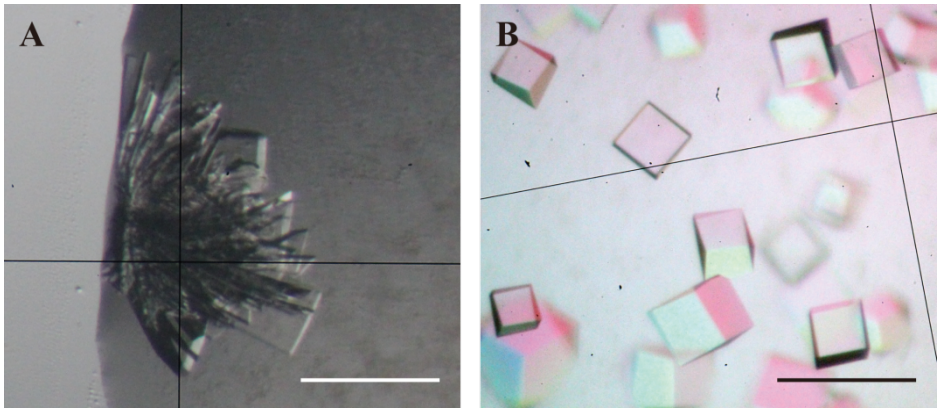

Figure II-1 Crystals of PB2 middle domain from H1N1. A) wild type crystals and B) double mutant (P453H, I471T) crystals. The bars represent 200 micrometer.

Table II-1 Data collection and structure refinement statistics of PB2 middle domain mutant

Data collection

	Apo form	m^7GTP-bound form
Unit cell (Å)	a=107.8, b=107.8, c=136.6	a=107.6, b=107.6, c=138.8
Space group	R32	R32
Beamline	Micro7HFM *RAXISVII*	Micro7HFM *RAXISVII*
Resolution (Å)	19.42-2.02 (2.09-2.02)	19.28-1.76 (1.82-1.76)
Total number of reflections	138,561(12,697)	209,190 (19,848)
Number of unique reflections	20,418 (1,964)	30,518 (2,993)
Completeness (%)	99.7 (96.9)	99.92 (99.73)
*R*merge	0.058 (0.791)	0.044 (0.598)
*R*meas	0.063 (0.862)	0.048 (0.649)
*R*pim	0.024 (0.338)	0.018 (0.250)
I/sigma(I)	24.9 (3.4)	34.0 (4.8)
Redundancy	6.79 (6.46)	6.85 (6.63)
$CC_{1/2}$	1.000 (0.711)	0.999 (0.817)

Refinement

*R*work	0.181	0.187
*R*free	0.227	0.223
RMSD bond length	0.007	0.007
RMSD bond angle	1.030	1.138
Number of atoms in the model	1,574	1,482
Number of water molecules	262	145
Number of residues in outlier region of Ramachandran plot	0	0
The average B-factor	33.5	34.2

Values in parentheses are for the last resolution shell.

$Rmerge = \sum hkl \sum i |Ii(hkl) - \langle I(hkl)\rangle| / \sum hkl \sum i Ii(hkl)$

$Rmeas = \sum hkl [N/(N-1)]^{1/2} \sum i |Ii(hkl) - \langle I(hkl)\rangle| / \sum hkl \sum i\, Ii(hkl)$

$Rpim = \sum hkl [1/(N-1)]^{1/2} \sum i |Ii(hkl) - \langle I(hkl)\rangle| / \sum hkl \sum i\, Ii(hkl)$

where $Ii(hkl)$ is the intensity measurement for a reflection hkl,

$\langle I(hkl)\rangle$ is the mean intensity for this reflection and N is Redundancy.

$CC_{1/2}$ is calculated according to the fomura in Ref. 21.

$Rwork = \sum hkl ||Fobs| - |Fcalc|| / \sum hkl |Fobs|$.

*R*free was calculated with randomly selected reflections (5%).

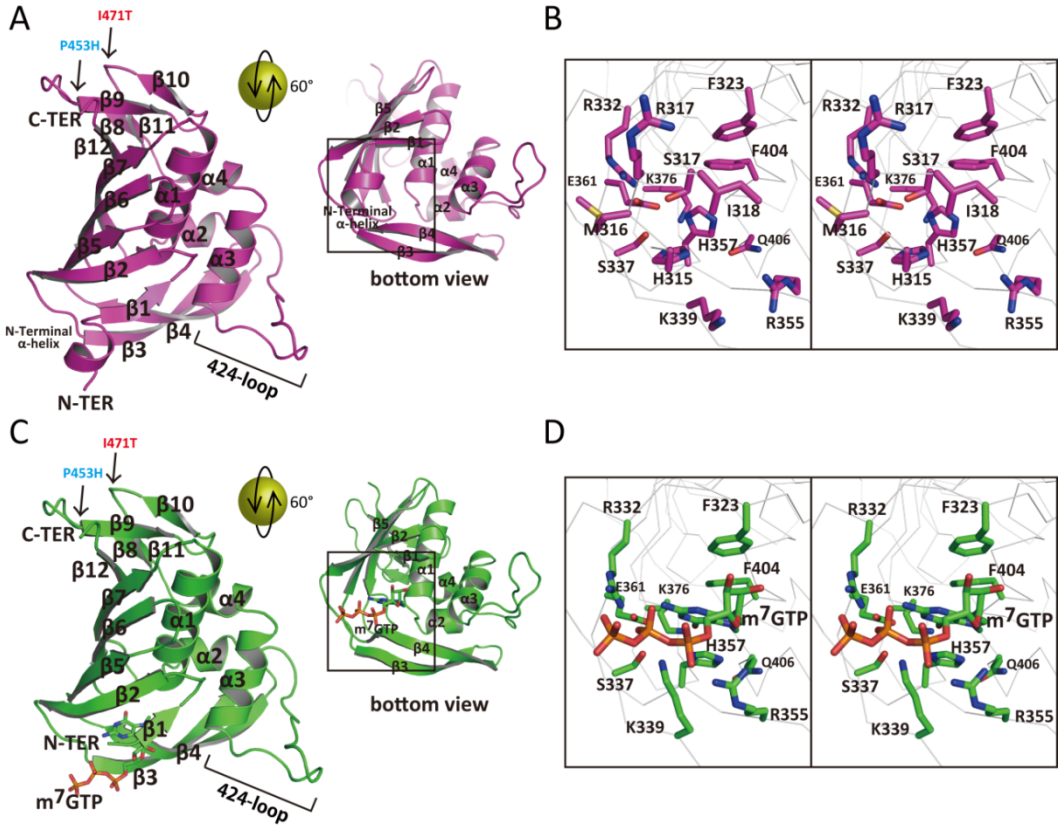

Figure II-2 Crystal structure of PB2 middle domain (amino acids 318 to 483) of H1N1 from human influenza with or without m^{7}GTP. A) Crystal structure without m^{7}GTP in magenta. Left panel is the overall structure. Right panel is the same model as left panel but rotated by 60° about a horizontal axis to show the active site. Secondary structures are labelled in black and two mutations P453H and I471T are indicated by arrows with blue and red labels, respectively. B) Close-up view of the square of panel A in stereo view. Main chain is represented by ribbon. Residues of active site and N-terminal helix are labelled in black. C) Crystal structure with m^{7}GTP in green. Left panel is the overall structure. Right panel is the same model as left panel but rotated by 60° about a horizontal axis to show the active site. to show the active site. m^{7}GTP is represented by stick model. Secondary structures are labelled in black and two mutations P453H and I471T are indicated by arrows with blue and red labels, respectively. D) Close-up view of the square of panel of C in stereo view. Main chain is represented by ribbon. Active site residues are labelled in black. H357, F404, E361 and K376 formed the active site cleft to bind to 7-methyl-guanosine. Triphosphate interact with R332, S337, K339, R355 and E361.

The side chain of His316 interacts with Ser336 and it seems to stabilize this α-helix. On the other hand, by m^{7}GTP soaking, the α-helix deformed to a flexible structure as describe later. The RMSD value is 1.00 Å between native and m^{7}GTP using all identical atoms. A homology structural search using DALI[75] showed no strong similarity with any other proteins except 2VQZ. This is also true for the PB2 large C-terminal domain, which shows no strong similarity to any other proteins. Apparently influenza A virus PB2 is very distant from other proteins, at least based on its structural classification.

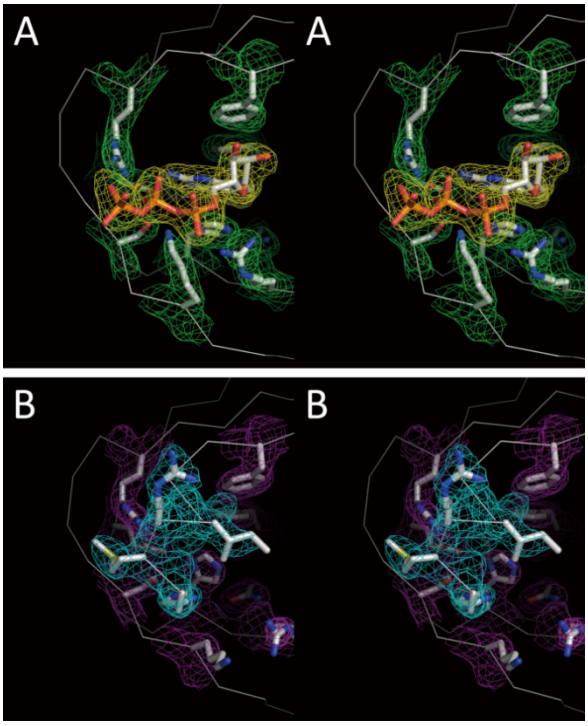

Figure II-3 Electron densities of the active sites in stereo view. The molecular orientation is the same as bottom view in Figure II-2. The 2Fo-Fc electron density maps are drawn at one sigma. A) The active site of m^{7}GTP-bound form. The electron density of m^{7}GTP and the active site residues are represented in yellow mesh and green mesh, respectively. B) The active site without m^{7}GTP. The electron density of additional N-terminal helix and the active site residues are represented in cyan mesh and magenta mesh, respectively.

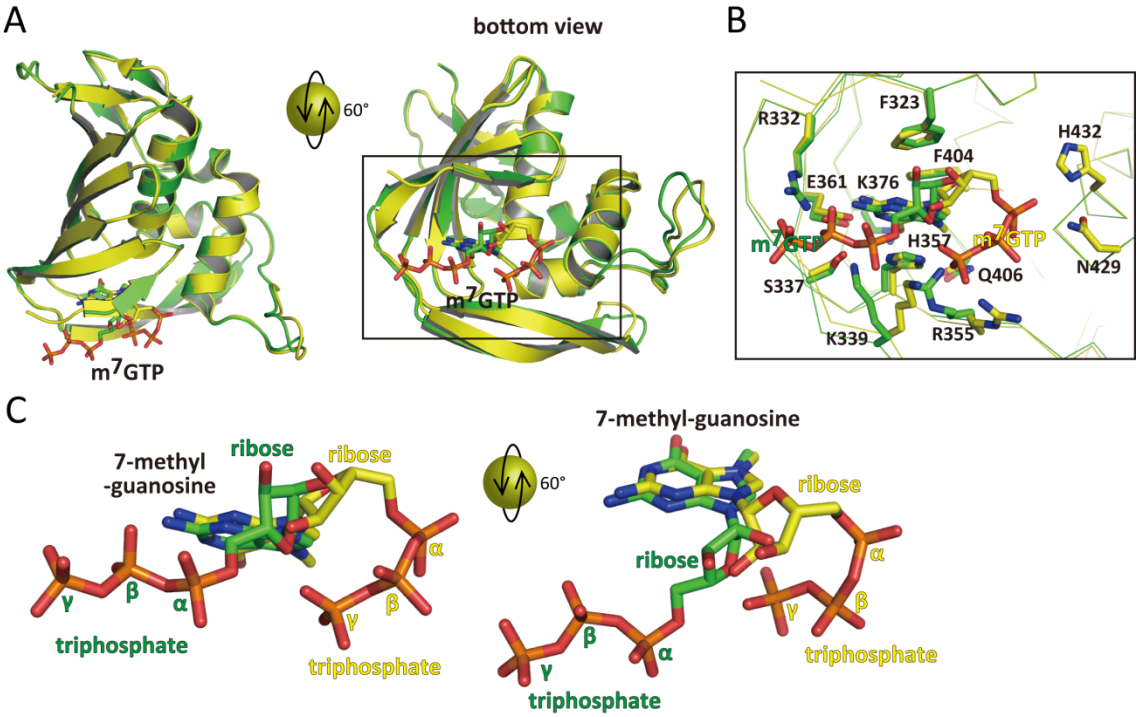

Figure II-4 Comparison the m^{7}GTP-bound form in H1N1 (this report) and H3N2 (2VQZ). A) Crystal structure in H1N1 and H3N2 are shown in green and yellow, respectively. Both m^{7}GTPs are depicted with stick model. Left panel is the overall structure and right panel is the bottom view with 60° orientation of left panel. B) Close-up view of the square of panel A. Main chain is represented by ribbon. Active site residues are labelled in black. C) Comparison the conformation of m^{7}GTP in H1N1 and H3N2 structure. Left panel is same orientation as A and B. Right panel is the same model as left panel but rotated by 60° about a horizontal axis to show the active site.. The position of ribose and triphosphate are labelled in each color. The 7-methyl guanosine is same conformation and it is labelled in black.

II.3.3 Conformational Polymorphism of m^{7}GTP

The crystal was soaked in 0.5 mM m^{7}GTP solution for 2.5 hours. The 2Fo-Fc electron density of m^{7}GTP was explicitly visible (Figure II-3). Compared with the reported structure (Figure II-4), it shows the similar conformation that 7-methyl-guanine is fixed in the deep cleft formed by His357, Phe404, Glu361 and Lys376. However, particularly significant change was seen in ribose and tri-phosphate region. In reported structure (2VQZ), the triphosphate is bent around the base with the α-phosphate interacting with His432 and Asn429 and the γ-phosphate interacting with His357 and, Lys339 and Arg355 (Figure II-4). In our structure, such bent could not be seen because the ribose rotated via N9 and C1 so the triphosphate continues directly to the outer domain (Figure II-2C, D left direction). Interestingly, compared with native structure, the N-terminal α-helix deformed to a flexible structure upon the soaking of m^{7}GTP, thus the tri-phosphate lies in the same region instead of α-helix. It is important to note that the N-terminal region is flexible with no electron density, it seemed that these N-terminal residues do not affect the conformation of m^{7}GTP. However, we can not deny the possibility that this N-terminal α-helix was artifact, because its component amino acids are derived from expression vector. Furthermore, in two more structures of PB2 middle domain with m^{7}GTP, all m^{7}GTP conformation is the same as that in 2VQZ[67]. Conformational features of the presented m^{7}GTP are listed as follows: (1) the side chain of Arg355 and Lys339 changed the direction to hold the triphosphate. The feature is not seen in other PB2 middle domain structures with m^{7}GTP. (2) The side chain of His357

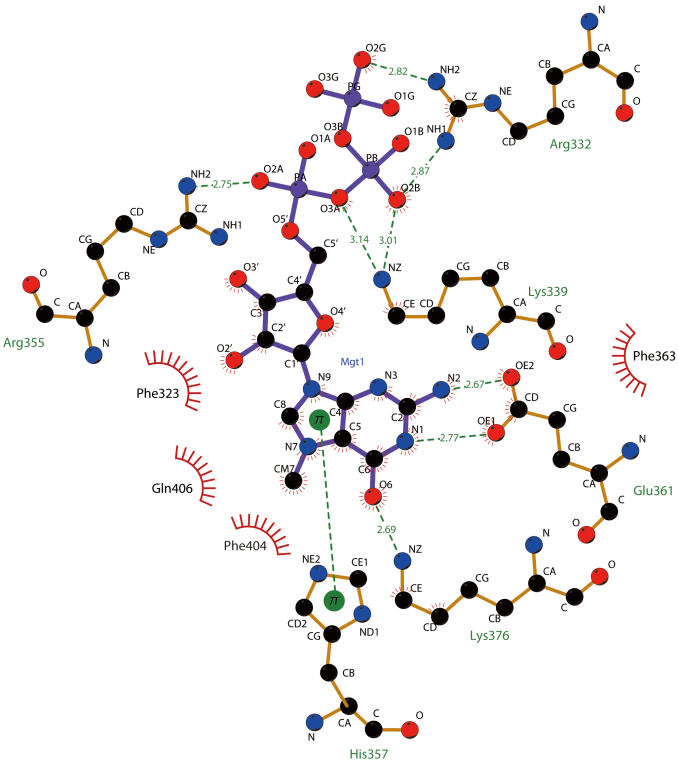

Figure II-5 Plan view of interactions between cap binding residues and m^{7}GTP. This figure is illustrated using Ligplot.

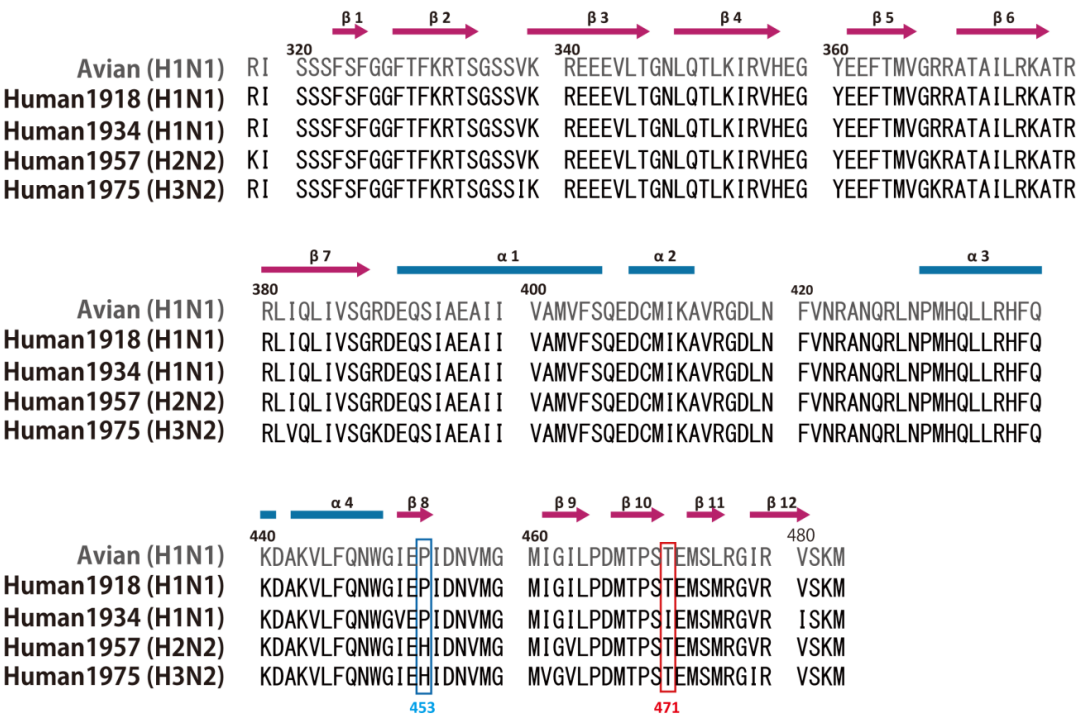

Figure II-6 Sequence alignment of the PB2 middle domains. Avian strain is shown in grey (A/mallard/Tennessee/11464/1985 (H1N1)). Human influenza virus is shown in black: H1N1 (A/Brevig Mission/1/1918), H1N1 (A/Puerto Rico/8/1934), H2N2 (A/Albany/20/1957), and H3N2 (A/Victoria/3/1975) as 2VQZ. The blue and red boxes are the mutation sites at 453 and 471 (See details in the text). Twelve ß-strands and four α-helices are depicted in hot pink arrows and light blue bar, respectively.

moves from apo to holo state to interact with five-membered ring of purine ring of 7-methyl-guanine via π-π interaction. (3) The conformation of m^7GTP in 2VQZ shows the interaction with Asn429, Met431 and His432, but the presented structure shows no interaction with these residues (Figure II-4, II-5).

II.4 Discussion

P453H mutation increased the surface basic electrostatic potential drastically

In Figure II-6, we showed the sequence differences of PB2 middle domain of avian influenza H1N1 and human influenza H1N1, H2N2 and H3N2. In the whole PB2 sequence, it was reported that seventeen substitutions, which are highly conserved in avian or human, would be candidates to enable to cross the barrier between the species from avian to human as an adaptive mutant[76]. In addition to the 17 characteristic sites, they reported that two more additional characteristic sites unique to the H1N1 (human), and nine unique to the HxN2 (H2N2/H1N2/H3N2, human). These eleven variants would be also candidates which are needed to cross the species barrier between avian H1N1 and human HxN2. There are no overlap between these sites and the former seventeen mutations[76]. Within former seventeen substitutions, seven sites at position 567, 588, 613,

627, 661, 674, and 702 are highly conserved in the C-terminal domain of PB2. Especially, at 627 position, glutamate is conserved in avian H1N1 with 99.31% and lysine is conserved in human H1N1 and HxN2 with 99.76%[76]. E627K mutation dramatically increased basic charge on the surface. It facilitated the adaptation of H5N1 and other avian viruses to mammals and increased their transmission and/or pathogenicity in humans, mice, ferrets and guinea pigs[77]. Within the PB2 middle domain, there are each two sites with the change from avian to human (residues 368 and 475 (1st human isolate in 1940 and 1918, respectively)) and from avian to H2N2/H3N2 (residues 382 and 453 (1st human isolate in 1961 and 1940, respectively))[76]. These sites are not in the vicinity of the cap-binding site. Among these four sites, the mutation at position 453 is particularly interesting because it is so drastic, going from proline (H1N1) to histidine (H3N2), though other mutations occur within similar character such as basic (R368K) or hydrophobic (I382V). The P453H mutation first appeared in 1940. Residue 453 is Pro (or Ser) with 98.29% conservation in avian H1N1, and His is conserved in human HxN2 with 99.49%. Thus, based on the characteristic features of P453H mutation, it might be more possible candidate than the others for an adaptive mutation from avian to human HxN2[76]. In this report, we observed that the PB2 middle domain with two mutations (P453H and I471T) change the solubility and finally we obtained good diffraction crystals by these mutations. It has been well known that the electrostatic surface change by the single E627K mutation enhanced the virulence[26], though it is still open question what is the role of Lys627 in the RNP complex. Whether the P453H mutation is linked to the viral specific feature of H2N2 or H3N2 is an important issue to be addressed. Given that the histidine at 453 is present in H2N2 or H3N2 but not H1N1, this site may contact with other components such as RNA, PB2, PB1, PA, NP and nuclear export protein[78].

Methylated group is necessary for substrate recognition

m^7GTP is bound in the cap binding site of PB2 middle domain by hydrophobic interactions, hydrogen bonds, ionic bonds, π-π interaction as shown in Figure II-5. Arg332, Lys339 and Arg355 interacted with oxygen atoms of tri-phosphate group and Glu336 and Lys376 interacted with guanine moiety. Furthermore, His357 interacted with guanine ring by π-π interaction and guanine moiety was located between His357 and Phe404.

We carried out crystal soaking using apo PB2 middle domain crystals with various GTP-analogs as the same method as m^7GTP. We used GTP, GTPγS, m^7G, m^7GMP, m^7GDP, m^7GP_5G, EDA-m^7GTP. From the results of X-ray diffraction analysis, the electron densities of methylated analogs (m^7G, m^7GMP, m^7GDP, m^7GTP, m^7GP_5G,

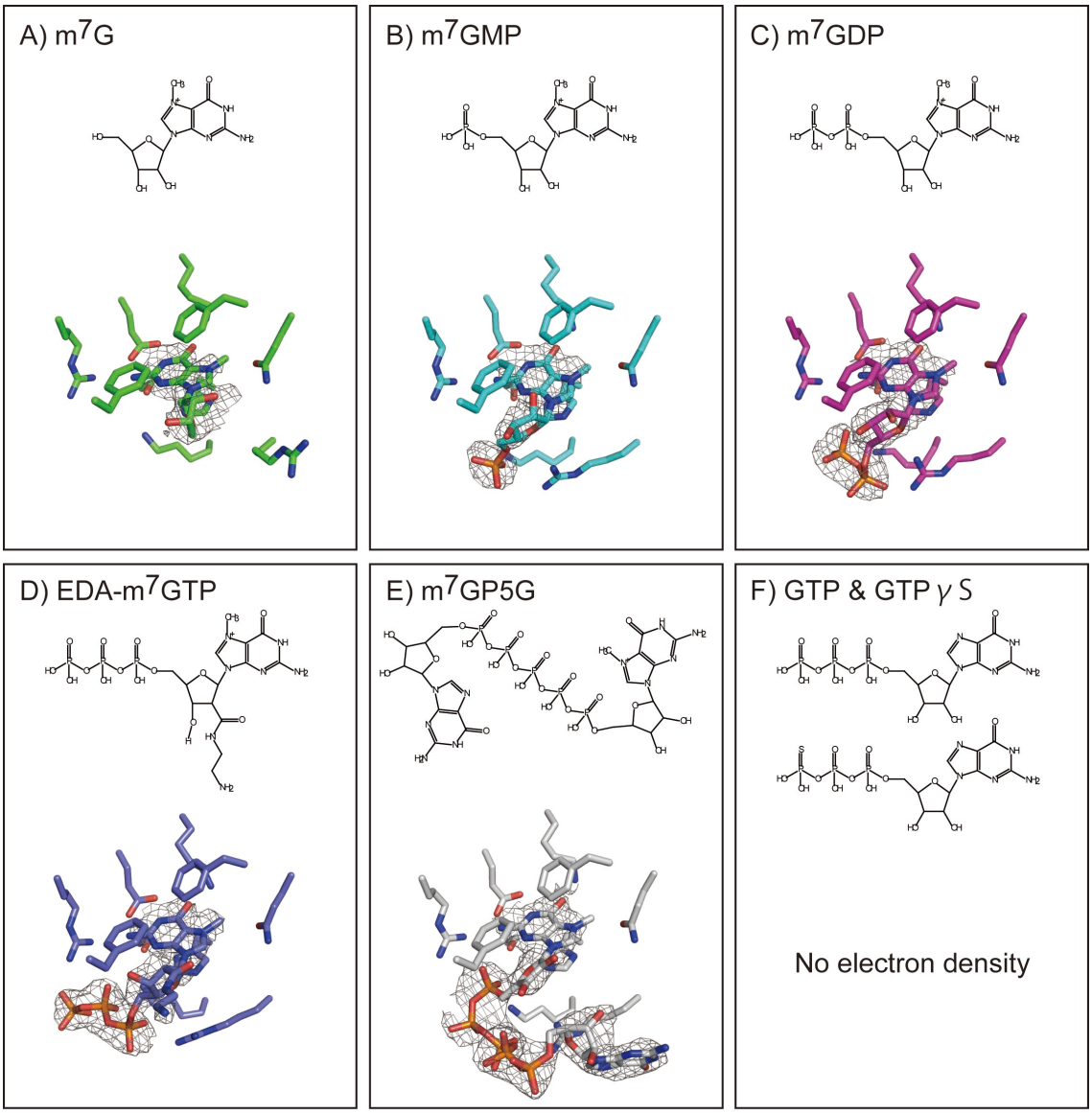

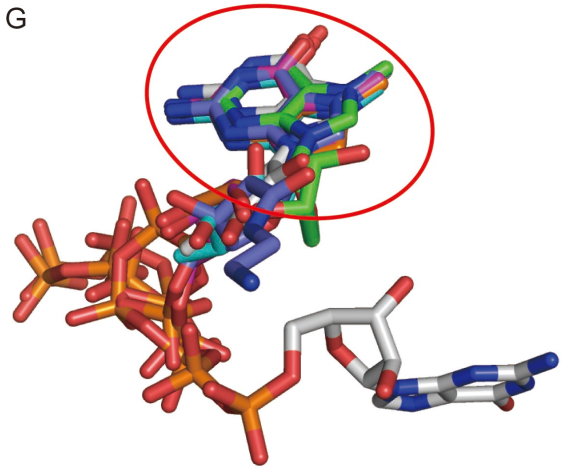

Figure II-7 Electron density of GTP analogs. A) m^7G, B) m^7GMP, C) m^7GDP, D) EDA-m^7GTP, E) m^7GP5G and F) non-methylated ligands, GTP and GTPγS. The 2Fo-Fc electron density maps are drawn at 1 σ. G) Superimposed model of observed ligands (A–E and m^7GTP). Red circle indicates guanine moiety, which is observed in almost same place.

EDA-m^7GTP) were observed in cap binding site, on the other hand, those of all non-methylated analogs (GTP and GTPγS) were not observed (Figure II-7A-E). Guanine moieties of observed structure located at same position (Figure II-7G).

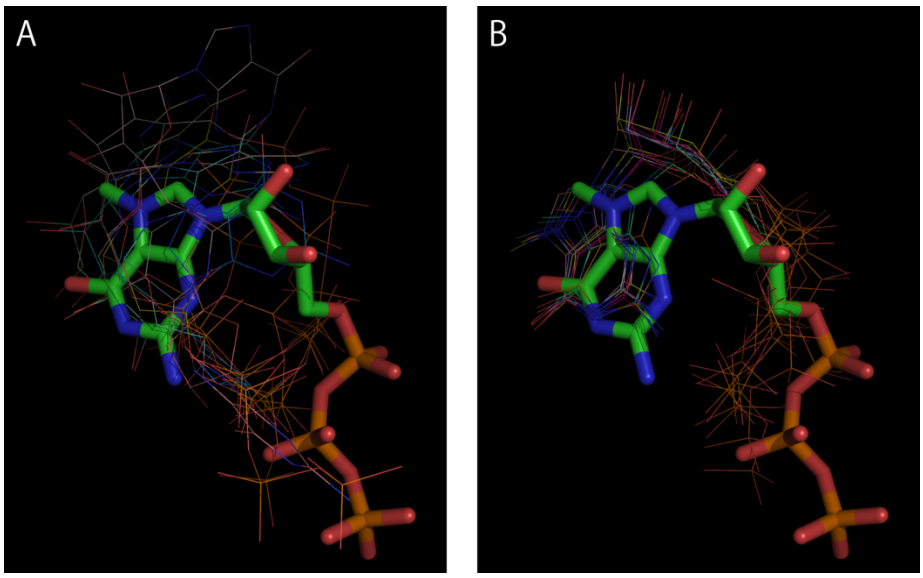

Figure II-8 Calculated candidates of GTP (A) and m^7GTP (B). Each ten candidates are calculated using Molegro Virtual Docker (Northern Science Consulting). Original m^7GTP, which we revealed, are depicted in stick model. Candidates are depicted in line model.

Then, we calculated the binding energy of PB2 middle domain-m^7GTP or -GTP using Molegro Virtual Docker (Northern Science Consulting). We used the GTP structure whose conformation was the same as m^7GTP without methylated group. The energy of m^7GTP binding (score = -221) was lower and more stable than that of GTP binding (score = -208). These scores are calculated based on the total energy of ligand-protein interaction and ligand itself when ligand binds to protein[79]. Furthermore, we simulated molecular docking of m^7GTP, or GTP, into apo PB2 middle domain structure. A hundred candidate conformations of each m^7GTP and GTP were calculated and we extracted best ten conformations of each. Average of ten RMSDs between original m^7GTP, which we revealed, and m^7GTP candidates was 3.8 Å and that between original m^7GTP and GTP candidates was 5.9 Å (Table II-2). Furthermore, we compared original m^7GTP conformation with these candidates. No GTP candidate overlapped with original m^7GTP and their guanine moieties were located in

Table II-2 RMSDs between original m^7GTP and candidates.

Rank	m^7GTP	GTP
1	3.83 (-217.5)	6.02 (-183.7)
2	3.78 (-217.1)	6.80 (-181.1)
3	4.31 (-204.2)	4.79 (-180.6)
4	3.90 (-203.6)	6.20 (-180.5)
5	4.44 (-202.9)	5.52 (-180.3)
6	2.09 (-201.1)	5.85 (-179.5)
7	2.80 (-198.9)	5.72 (-177.6)
8	2.64 (-195.9)	6.78 (-177.4)
9	3.77 (-195.4)	6.30 (-177.4)
10	6.04 (-195.0)	5.06 (-177.0)
Average	**3.76**	**5.90**

RMSDs were calculated using Molegro Virtual Docker (Northern Science Consulting). Values in parentheses are Moldock scores.

the cavity randomly (Figure II-8A). However, m^7GTP candidates converged at similar position as original m^7GTP including guanine moiety, methylated group and especially monovalent nitrogen atom (N7) of m^7GTP (Figure II-8B). Whereas this monovalent nitrogen may interact with Phe404 by CH-π interaction[80], there is no CH-π interaction between cap binding residues and GTP. It is indicated that m^7GTP specifically bind in the cavity via methylated group and monovalent nitrogen by CH-π interaction. These results suggest that PB2 middle domain distinguishes host messenger RNAs from other RNAs with methylated group or without it.

Importance of m^7GTP Conformation in the trimeric RNA-polymerase Complex

The novel conformation of m^7GTP we presented will be important clue for drug design targeting the cap-binding site. It should be noticed again that two mutations (P453H and I471T) we introduced are totally opposite surface against cap-binding site, thus they does not influence the conformational polymorphism of m^7GTP (original (2VQZ)[67] and novel site (this report)).

As we applied m^7GTP by crystal soaking, the conformation of soaked compound may be restricted by crystal packing. Thus we checked next points about the phosphate binding site: (1) Original site was preserved in our crystal statically: 7-methyl guanine occupies the same site, but phosphate binds in different manner. There is no direct disturbance to bind phosphate in original site in our crystal. In the original site, important residues for the phosphate binding (His432 and Asn429) did not change the position. (2) Original site was preserved in our crystal dynamically: In comparison with B-factor plot of four different PB2 structure with m^7GTP, there are two regions (338 region and 424 loop region) with large difference (Figure II-9A). It is considered that these regions are candidate which are influenced by crystal packing. In the same figure, the binding residues were plotted. It shows the phosphate binding site (His432 and Asn429) are not influenced because they are outside the 338 and 424-loop region. Furthermore, though the phosphate binds Arg332, Ser337 and Lys339 on the 338 region in our structure, we checked that the 338 region of our crystal is not restricted by molecular packing. Based on these facts, we concluded that the novel site is not artifact by the soaking and crystal packing.

In our crystal, there was less interaction between the molecules because solvent content is 70%. On the other hand, in other crystals (2VQZ and E4S5), the solvent contents are ~54%. Average B-factor of our crystal might be the relatively high B-factor compared with 4ES5 (H5N1), but is almost similar compared with 4EQK (H3N2) (Figure II-9A, B). This is the first report with or without m7GTP using the same crystal form. B-factors of

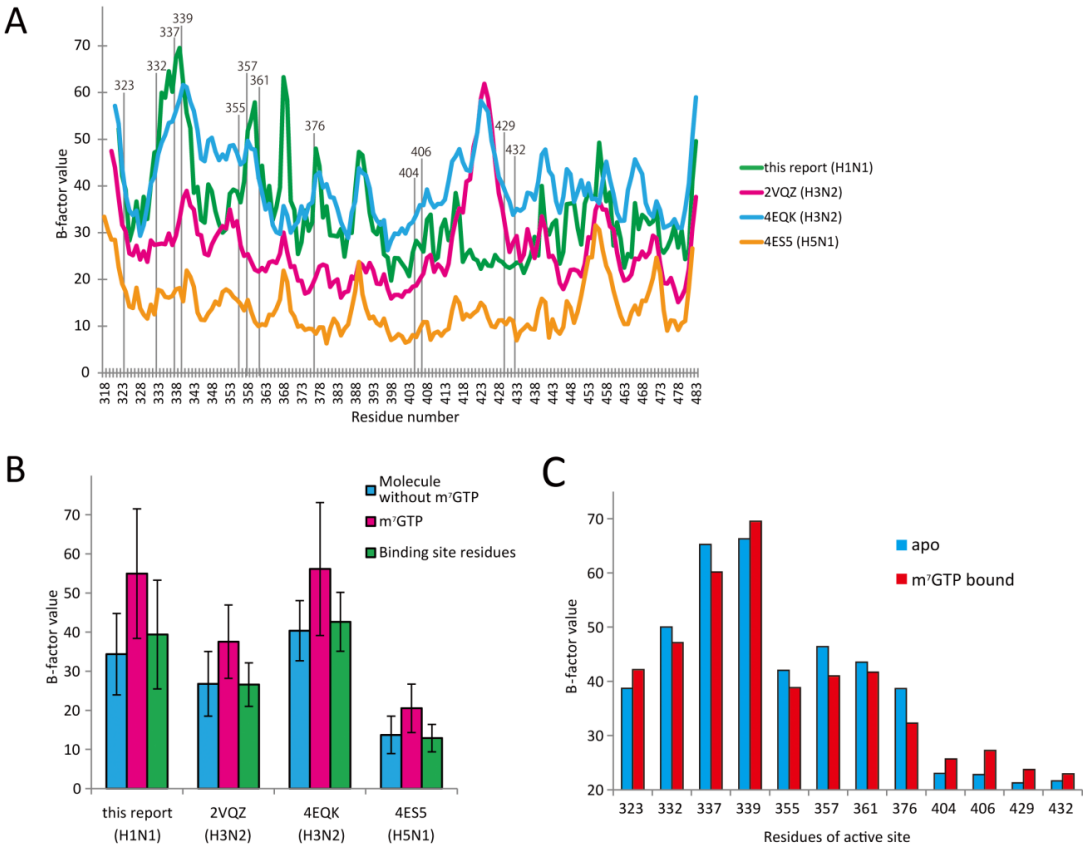

Figure II-9 B-factor plots of PB2 middle domain. A) B-factor plot for Cα carbons in m^7GTP-bound structures: B-factor of the structure in this report is plotted in green, 2VQZ is in magenta, 4EQK is in cyan and 4ES5 is in orange. Active site residues are indicated by vertical lines and labeled in black. B) Mean B-factor values of whole molecule without m^7GTP (cyan), m^7GTP only (magenta) and active site residues bound to m^7GTP (green). C) Changes of B-factor values of the active site residues between apo (blue) and m^7GTP (red).

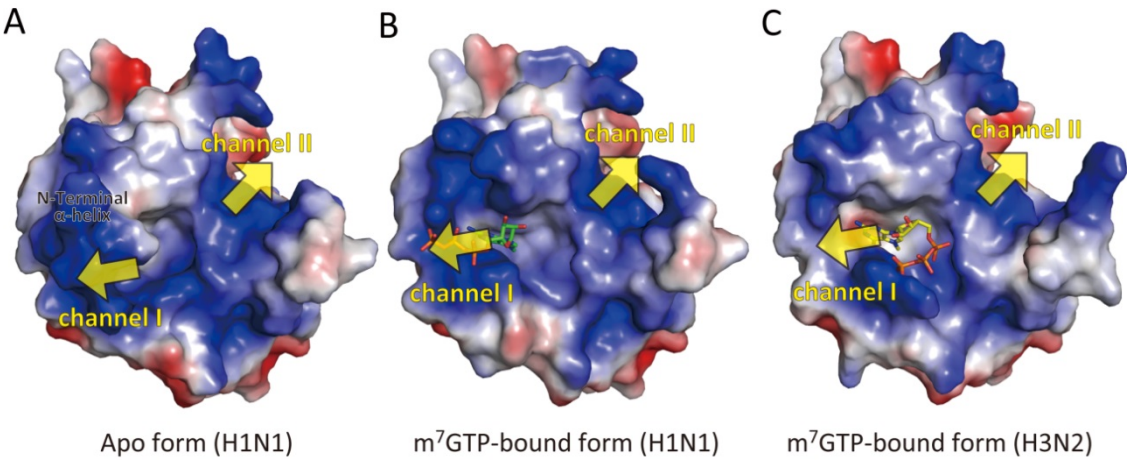

Figure II-10 Electrostatic surfaces of the PB2 middle domain. A) Apo form and B) m^7GTP-bound form in H1N1 and C) m^7GTP-bound form in H3N2. The molecular orientation is the same as bottom view in Figure II-2 and Figure II-4. Yellow arrows show the channels, which might bind the continuous RNA. Electrostatic surfaces were calculated and displayed using PyMOL.

some residues around m^7GTP (S332, S337, R355, H357, E361 and K376) are suppressed upon m^7GTP binding (Figure II-9C). In the first PB2 middle domain structural paper, it suggested the possibility of the different conformation of triphosphate in the context of a capped oligonucleotide. In electrostatic surface of the cap-binding site (Figure II-10), we could see channels with strong basic charge in two regions. One region includes R335, K339, K331 and R332 (channel I) and the other region includes R423 on the 424-loop, R436 and R368 (channel II). We observed that the capped-oligonucleotide interacts with channel I in the conformation, but we do not deny the possibility the continuous RNA interacts with channel II in the trimeric RNA-polymerase complex (Figure II-10). We still don't know which way the capped-oligonucleotide goes through in the trimeric RNA-polymerase complex and this will be next important issue to be addressed.

Chapter III:

Arginine ADP-ribosylation mechanism of iota-toxin from *Clostridium perfringens*

III.1 Introduction

Clostridium perfringens iota-toxin (Ia) mono-ADP-ribosylates Arg177 of actin, leading to cytoskeletal disorganization and cell death. Ia is known to contain three conserved regions: an aromatic residue-R/H, an EXE motif and a STS motif (Figure III-1). The EXE motif, which is on the ADP-ribosylating turn-turn (ARTT) loop is particularly important for the enzyme activity and has been investigated in point mutation and crystallography studies[42]. Still, the available information on the structural basis of the catalytic mechanism of ARTs remains limited and incomplete because of the limited information on the ART-substrate protein complex. To fully understand the reaction mechanism of arginine specific mono-ADP-ribosyl transferase, the structure of the toxin substrate protein complex must be characterized.

To understand the mechanism underlying molecular recognition and arginine ADP-ribosylation by ART, Tsuge et al. recently reported the crystal structure of the Ia-actin complex using a non-hydrolyzable NAD^+ analog, thiazole-4-carboxamide adenine dinucleotide (βTAD)[52]. The structure of the complex revealed the mechanism of Ia-actin recognition and suggests a possible reaction mechanism. However, the structures of the NAD^+-bound form (NAD^+-Ia-actin) and the ADP-ribosylated form (Ia-ADP-ribosylated (ADPR)-actin) remain unclear.

Accidentally, we obtained the crystals of Ia-actin complex without ligand (apo-Ia-actin) and found that ethylene glycol as cryo-protectant inhibits ADP-ribosylation and crystallized the NAD^+-Ia-actin complex. Here we report high-resolution structures of NAD^+-Ia-actin and Ia-ADPR-actin obtained by soaking apo-Ia-actin crystal with NAD^+ under different conditions. The structures of NAD^+-Ia-actin and Ia-ADPR-actin represent the pre- and postreaction states, respectively. By assigning the βTAD-Ia-actin

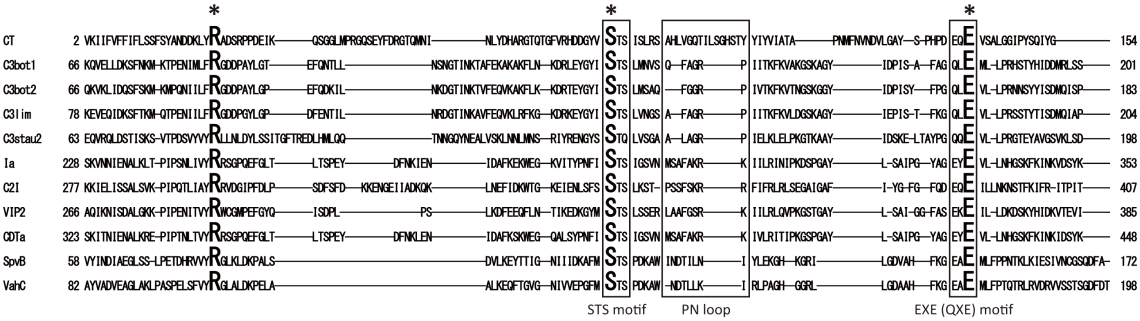

Figure III-1 Sequence alignment of ARTCs; CT, C3bot1, C3bot2, C3lim, Iota (Ia), C2I, VIP2, CDTa, SpvB and VahC. ARTCs have R-S-E motifs which are depicted in large characters with asterisks. The regions of interest are highlighted in squares; these include STS motif, PN loop and EXE (QXE) motif.

structure to the transition state, the strain-alleviation model of ADP-ribosylation, which Tsuge et al. proposed previously[52], is experimentally confirmed and improved. Moreover, this reaction mechanism appears to be applicable not only to Ia but also to other ADP-ribosyltransferases.

III.2 Materials and Methods

III.2.1 Sample preparation, crystallization, and NAD+ Soaking

Iota-toxin (Ia) purified from *Bacillus subtilis* contaminated small amounts of protease, which caused actin cleavage in the DNaseI-binding loop. Ia did not cause the cleavage in the thiazole-4-carboxamide adenine dinucleotide (βTAD)-Ia-actin structure reported previously; however, we used *Escherichia coli* (pET15b)-produced Ia in this report. BL21 (DE3) cells transformed with pET15b-Ia were selected on LB plates with ampicillin. A single colony was inoculated into 5 mL of LB and grown until A600 of ~0.5. The culture was transferred into 1 L of LB–ampicillin and grown overnight with vigorous shaking at 37 °C. Cells were harvested by centrifugation at 4 °C at 8,000 × g for 5 min and resuspended in 50 mL of buffer [20 mM Tris・HCl (pH 8.0), 500 mM NaCl, 20 mM imidazole, complete EDTA-free (Roche)]. Cells were passed through a French press and centrifuged at 13,000 × g for 30 min. The supernatant was loaded onto Ni-NTA agarose, and the elution fraction was dialyzed against buffer A [10 mM Tris・HCl (pH 8.0)]. The sample was loaded onto a Q Sepharose column (Bio-Rad) equilibrated with buffer A and eluted using buffer A plus 1 M NaCl. The eluate was dialyzed overnight against 10 mM Tris-HCl (pH 8.0). Ia concentrated to 15 mg/mL by ultrafiltration and stored at −70 °C. Ia from *E. coli* includes five extra N-terminal residues: RGSHM. We used newly purified Ia to make a large crystal. In addition, E378S, E380A, and E380S mutants of Ia were prepared using the same protocols. Actin preparation was described previously[52]. Basically, crystallization of apo-Ia-actin and NAD+-Ia (mutants)-actin was described before using the same protocols as prepared for βTAD-Ia-actin[52]. Latrunculin A was used

for the purpose of stabilizing the monomeric state of actin. Apo-Ia-actin crystals were obtained by hanging drop vapor diffusion in 100 mM MES (pH 6.5) and 18 - 20% PEG1,500 at 4 °C. To obtain larger apo-Ia-actin crystals, both micro and macro seeding were applied. NAD+ soaking of apo-Ia (WT)-actin crystals was done under two conditions (Figure III-2). The first condition (10 mM NAD+ soaking in cryo-protectant 30% (v/v) ethylene glycol for 30 min at room temperature) made NAD+-Ia-actin. The second condition (10 mM NAD+ soaking in crystallization mother liquor for 30 min at room temperature) made Ia-ADP-ribosylated (ADPR)-actin.

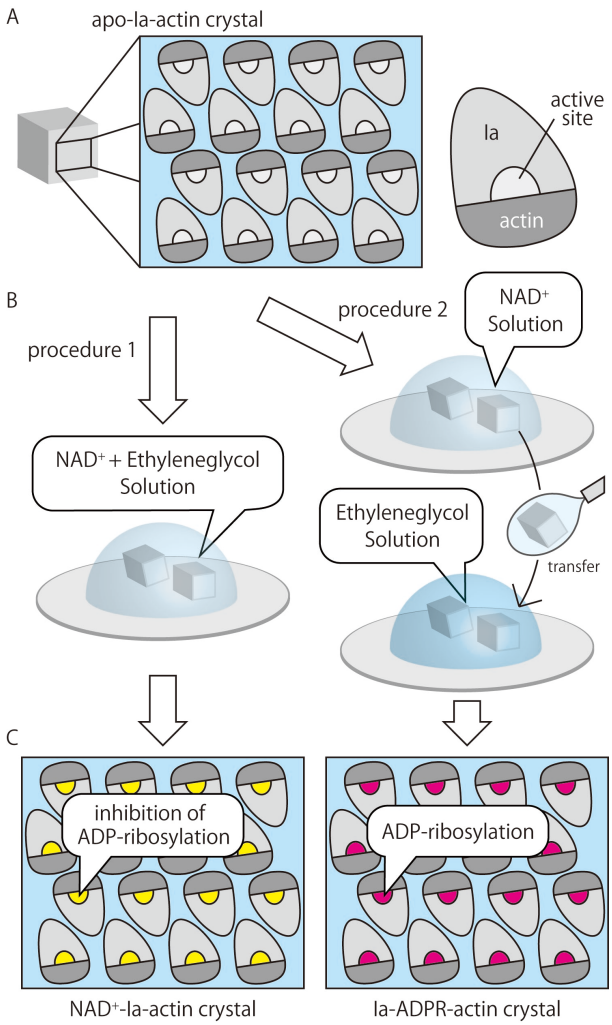

Figure III-2 Soaking method to create NAD+ binding Ia-actin complex and Ia-ADPR actin from common apo-Ia-actin crystal. A) apo-Ia-actin crystal. B) two procedures of crystal soaking into NAD+ and/or cryoprotectant solution. C) NAD+-Ia-actin crystal from procedure 1 (left) and Ia-ADPR-actin crystal from procedure 2 (right).

III.2.2 Data collection and model building

Each crystal was picked up using a nylon loop, dipped in mother liquor supplemented with 30% ethylene glycol as a cryoprotectant, and plunged into a nitrogen-gas stream at 100 K. The crystal space group was determined to be $P2_12_12_1$, and the crystal packing of Ia and actin was basically the same as in βTAD-Ia-actin. Data collection statistics, cell constants, and the final model statistics of apo-Ia-actin, NAD+-Ia (WT and mutants)-actin, and Ia-ADPR-actin are summarized in Tables III-1 and III-2 as follows. Data collection was done at 100 K using an X-ray wavelength of 1.0 Å on the PF-AR NW12A and BL5A beamlines at KEK Photon Factory, using a Quantum 210r detector system. A total of 540 frames were collected with 0.3° oscillations. This strategy yielded high-resolution data sets with high quality beyond 2 Å, especially for NAD+-Ia (WT)-actin. The diffraction images were integrated and scaled using the programs DENZO and SCALEPACK from the HKL-2000 suite[56].

Table III-1 Data collection and structure refinement statistics of Ia-actin complexes

	apo-Ia-Actin	NAD^+-Ia-Actin	Ia-ADPR-Actin
Unit cell (Å)	a = 53.9, b = 135.0, c = 154.5	a = 54.4, b = 135.9, c = 153.10	a = 54.0, b = 134.2, c = 151.0
space group	$P2_12_12_1$	$P2_12_12_1$	$P2_12_12_1$
Beamline	PF-AR NW-12	PF BL-5A	PF BL-5A
Resolution (Å)	50.0 - 2.7	50.0 - 1.75	50.0 - 2.20
Number of reflections	31,910 (1,539)	110,554 (5,154)	56,709 (2,789)
Completeness	99.8 (99.5)	96.4 (90.9)	99.9 (99.6)
Rsym	0.076 (0.390)	0.040 (0.351)	0.040 (0.327)
I/sigma	9.9	19.9	13.7
Redundancy	7.1	5.5	7.2
Rwork/Rfree	0.224 / 0.262	0.216 / 0.233	0.212 / 0.239
rmsd Bond length / Bond angle	0.008 / 1.332	0.006 / 1.420	0.006 / 1.472

Values in parentheses are for the last resolution shell.
Rsym = $\sum h \sum i |Ii(h) - \langle I(h)\rangle| / \sum h \sum i |Ii(h)|$, where $Ii(h)$ is the intensity measurement for a reflection h, and <I(h)> is the mean intensity for this reflection.
Rwork= $\sum h ||Fobs| - |Fcalc|| / \sum h |Fobs|$.
Rfree was calculated with randomly selected reflections (5%).
All structure have no residue in outlier region analyzed with Ramachandran plot

Table III-2 Data collection and structure refinement statistics of Ia (mutant)-actin complexes

	NAD^+-IaE378S-Actin	NAD^+-IaE380A-Actin	NAD^+-IaE380S-Actin
Unit cell (Å)	a = 53.9, b = 134.9, c = 153.9	a = 54.0, b = 134.2, c = 151.1	a = 53.9, b = 134.9, c = 154.3
space group	$P2_12_12_1$	$P2_12_12_1$	$P2_12_12_1$
Beamline	PF BL-5A	PF BL-5A	PF BL-5A
Resolution (Å)	50.0 - 2.03	50.0 - 2.36	50.0 - 1.94
Number of reflections	71,718 (3,382)	47,500 (1,949)	83,852 (4,100)
Completeness	97.6 (92.3)	97.3 (92.0)	99.9 (99.5)
Rsym	0.038 (0.322)	0.051 (0.191)	0.063 (0.292)
I/sigma	17.0	24.9	29.6
Redundancy	6.1	6.4	5.3
Rwork/Rfree	0.215 / 0.234	0.224 / 0.251	0.219 / 0.233
rmsd Bond length / Bond angle	0.006 / 1.438	0.007 / 1.343	0.006 / 1.624

Values in parentheses are for the last resolution shell.
Rsym = $\sum h \sum i |Ii(h) - \langle I(h)\rangle| / \sum h \sum i |Ii(h)|$, where $Ii(h)$ is the intensity measurement for a reflection h, and <I(h)> is the mean intensity for this reflection.
Rwork= $\sum h ||Fobs| - |Fcalc|| / \sum h |Fobs|$.
Rfree was calculated with randomly selected reflections (5%).
All structure have no residue in outlier region analyzed with Ramachandran plot

The structures of apo-Ia-actin and NAD^+-Ia (WT and mutants)-actin were determined using the molecular replacement method with MOLREP[81,82] in CCP4i in the structure of ßTAD-Ia-actin (3BUZ) in which ßTAD, ATP, Latrunculin A, calcium, and waters were deleted. Each structure was refined using REFMAC5[81,82] rigid body refinement because the relative positions differed. Thereafter, the model structure was refined iteratively

using REFMAC5 restraint refinement and Coot[71]. Finally, cofactors (NAD^+, ATP, Latrunculin A, calcium) and waters were added. Comparison of the structures was done using PyMOL[72]. The structure of Ia-ADPR-actin was determined in the same manner, and the ADP-ribosylated arginine cif file was built using PRODRG[83].

III.2.3 Assay of ADPRTase and NADase Activity

ADPRTase Activity assay; The crystal assay was conducted as follows: crystals of the Ia-actin complex were washed with mother liquor twice. Biotin-NAD^+ (50 μM) was added to the mother liquor containing the Ia-actin complex, and the mixture was kept at room temperature overnight. These samples were then subjected to SDS-PAGE. The gel was washed twice with PBS, stained with streptavidin-FITC (250 nM), washed twice with PBS again, and scanned using a Typhoon FLA9000 (General Electric). The solution assay was conducted as follows: Ia (1.6 μM) and actin (8 μM) were mixed together in mother liquor. Biotin-NAD^+ (10 μM) was then added to the mixture, which was kept at room temperature overnight. Thereafter, the same protocol used for the crystal assay was applied.

NADase Activity assay; Samples were prepared with 500 μM NAD^+ added to 10 μM (final concentration) Ia and incubated at 37 °C for 1 h. We carried out NADase activity assay by FPLC-equipped TSK-GEL column (Tosoh) with running buffer containing 100 volumes of 20 mM phosphate buffer (pH 5.5) and 5 volumes of acetonitrile at room temperature. The authentic ligands, such as NAD^+, ADP ribose, and nicotinamide, were analyzed alone with 1 mL/min flow rate. Mixtures of enzyme and NAD^+ were analyzed in the same condition.

III.3 Results

III.3.1 Structures of Ia-Actin complexes

To investigate the reaction mechanism underlying ART-catalyzed arginine ADP ribosylation, our aim was to examine structural snapshots obtained during the reaction from NAD^+ to ADPR-arginine. Unfortunately, co-crystallization of the NAD^+-Ia-actin complex failed because ADP-ribosylation proceeded in the crystallization buffer. However, we were able to produce small apo-Ia-actin crystals, after which we refined the crystallization conditions to grow larger crystals. The structure of apo-Ia-actin was solved by molecular replacement using βTAD-Ia-actin as a model (Figure III-3A). Although the relative orientation of apo-Ia-actin differs slightly from βTAD-Ia-actin, the

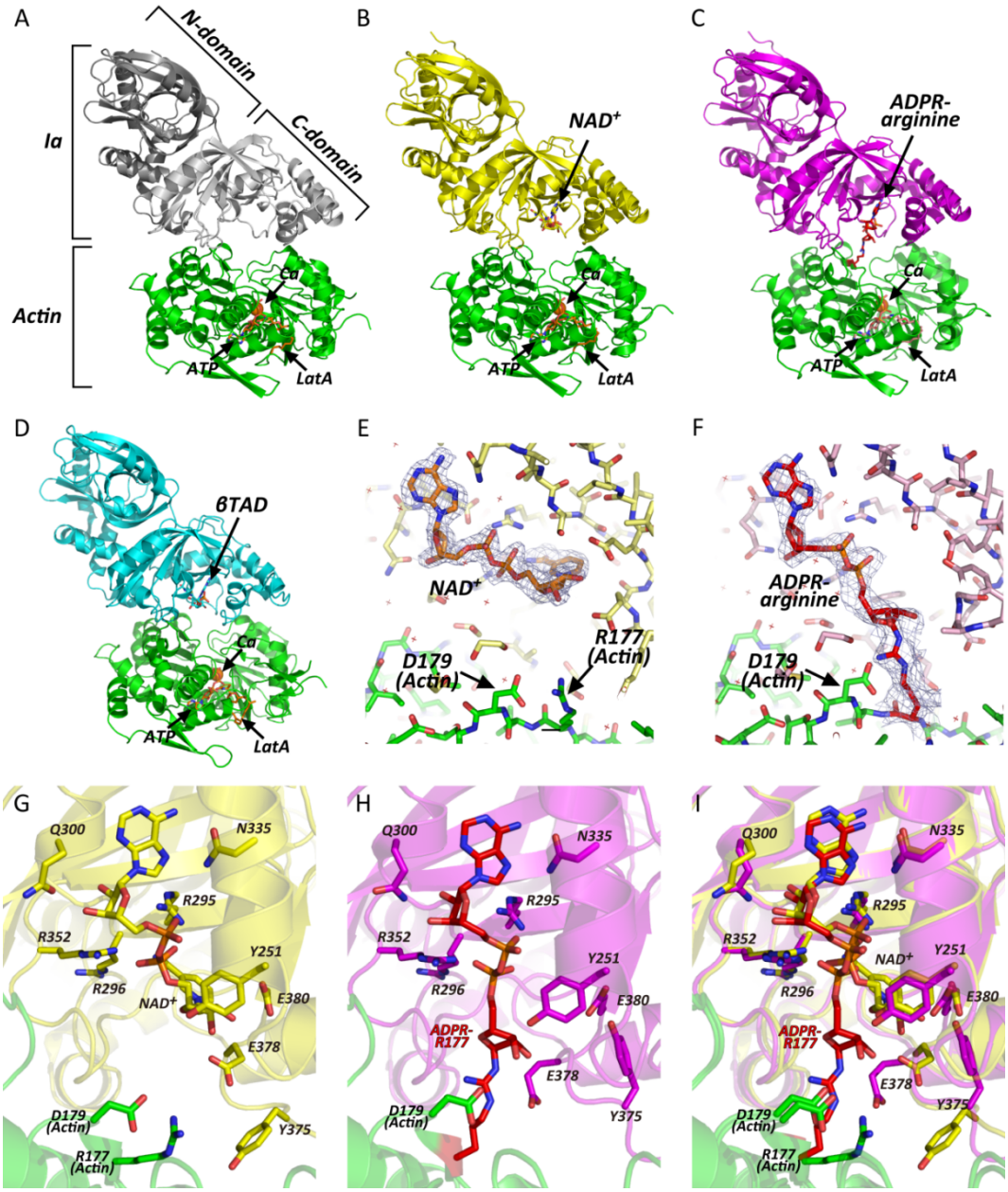

Figure III-3 Overall structures of Ia-actin complex during the reaction. A) Apo-Ia-actin; Ia is depicted in white as the C domain and gray as the N domain. B) NAD^+-Iaactin; Ia and NAD^+ are in yellow. C) Ia-ADPR-actin; Ia is in magenta and ADP-ribosylated R177 is in red. D) βTAD-Ia-actin (25); Ia and βTAD are in cyan. All actins are in green. NAD^+, ADPR-arginine, ATP, and latrunculinA (LatA) are represented in stick formation. Calcium (Ca) is represented as a sphere. E, F) Electron density around NAD^+ within the NAD^+-Ia-actin and around ADPR-arginine within the Ia-ADPR-actin complex. NAD^+, R177/ADPR-R177, and D179 of actin are labeled. The 2Fo-Fc electron density maps are drawn at 1 σ. G) Close-up view of NAD^+-Ia-actin. (H) Close-up view of Ia-ADPR-actin. (I) Superposed view of NAD^+-Ia-actin and Ia-ADPR-actin: all colors are the same as in B) and C). Side chains of R177 and D179 in actin are depicted and labeled. In Ia, Y251, R295, R296, Q300, N335, R352, Y375, E378, and E380 are labeled.

basic structural framework of the complex was retained, which is necessary for the ADP-ribosyltransferase reaction. This suggests that the unique apo-Ia-actin complex crystal can be thought of as a reaction chamber for the examination of ADP-ribosylation reaction and the structural changes that occur upon ADP-ribosylation.

By soaking the apo-Ia-actin crystals with NAD^+ under different conditions, we obtained data sets of NAD^+-Ia-actin and Ia-ADPR-actin at 1.75 and 2.2 Å resolution, respectively (Table III-2). Specifically, soaking apo-Ia (WT)-actin crystals with 10 mM NAD^+ in cryo-protectant containing 30% ethylene glycol for 30 min at room temperature yielded NAD+-Ia-actin, whereas soaking the complex with 10 mM NAD^+ in mother liquor for 30 min at room temperature yielded Ia-ADPR-actin. Overall, the structures of apo-Ia-actin, NAD^+-Ia-actin, and Ia-ADPR-actin were similar to βTAD-Ia-actin, but there were obvious differences around the NAD^+-binding site (Figure III-3A-D). With NAD^+-Ia-actin, the difference map showed a clear NAD^+ electron density (Figure III-3E). With Ia-ADPR-actin, the 2Fo-Fc (Fo: observed intensity and Fc: calculated intensity) maps showed obvious differences from NAD^+-Ia-actin, including the presence of an ADP-ribosylated arginine density instead of NAD^+ (Figure III-3F).

In NAD^+-Ia-actin, the NAD^+ conformation is highly folded, as is seen in all ARTs. That is, the ADP moiety was gripped by Ia via Asn335, Gln300, Arg295, and Arg352, and the folded nicotinamide makes a hydrogen bond with the Arg296 main chain carbonyl and nitrogen (Figure III-3G-I). In Ia-ADPR-actin, the ADP moiety is gripped by the same residues as in NAD+-Ia-actin, but the N-ribose was largely moved to Arg177 of actin after nicotinamide cleavage (Figure III-4). It is important to note that there are no water molecules close to NC1 of N-ribose, which suggests that actin binding prevents unfavorable reactions as NADase from proceeding by making water molecules unavailable.

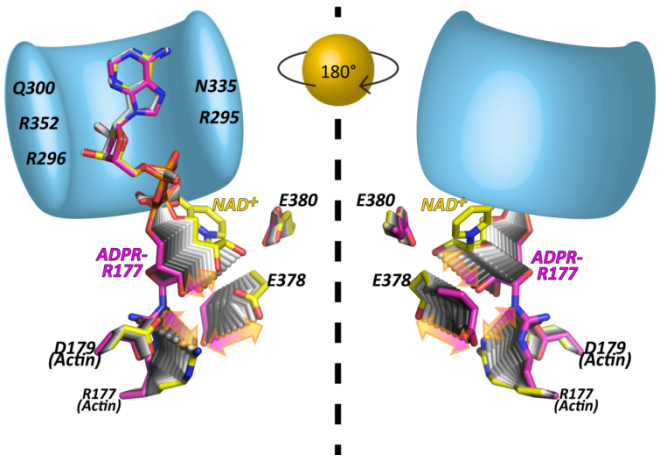

Figure III-4 Transient structures of the pre-reaction state [NAD^+-Ia-actin (yellow)] and the postreaction state [Ia-ADPR-actin (magenta)]. Schematic presentation of Ia (bright blue: R295, R296, Q300, N335, and R352 are labeled) gripping the ADP moiety of NAD^+ or ADPR. The Right panel is a back view of the Left panel.

The electrostatic molecular surface was shown in each state of the Ia-actin complex (Figure III-5). A key feature is that the

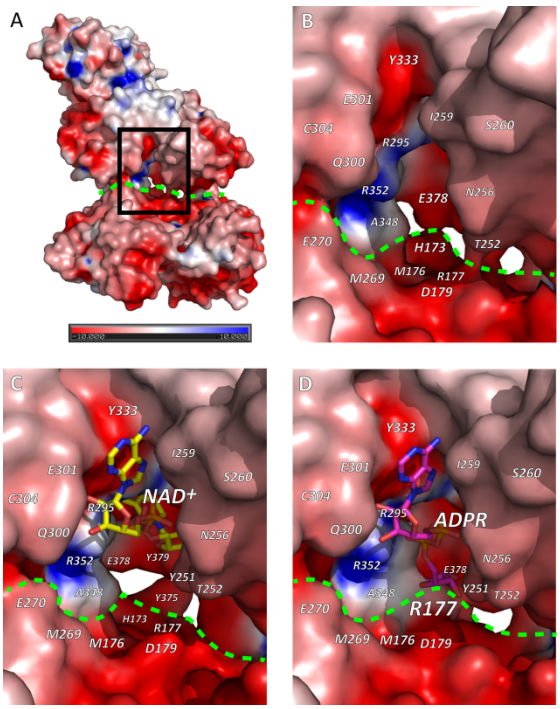

Figure III-5 Electrostatic molecular surfaces. A) the whole structure of apo-Ia-actin. Black square is the area in B-D. B) Close-up view of active site of Ia in apo-Ia-actin. C) Close-up view of active site of Ia in NAD+-Ia-actin. D) Close-up view of active site of Ia in Ia-ADPR-actin. NAD+ and ADPR are shown in stick representation. Dashed bright green line denotes interface between Ia and actin. Electrostatic molecular surfaces were calculated by GRASP and drawn using PyMOL.

Figure III-6 Detection of ADP-ribosylated actin. (A) ADP-ribosylation assay in apo-Ia (WT or mutant)-actin crystals. ADP-ribosylation occurs in the WT complex but not in the mutant complex. (B) Dose-dependent inhibition of ADP-ribosylation by ethylene glycol.

surface potential is acidic around NAD+ in NAD+-Ia-actin and Ia-ADPR-actin. It seems to stabilize two oxocarbenium ion intermediates as described later. When comparing the NAD+-Ia-actin and Ia-ADPR-actin complexes, another important difference could be seen at Arg177 of actin. Within the ADP-ribosylated actin, the side chain of Arg177 was tilted slightly and interacted covalently with ADPR (Figure III-3). By contrast, in apo-Ia-actin and NAD+-Ia-actin, Arg177 clearly interacted with Asp179 of actin by ionic bond. Using streptavidin-FITC and biotin-NAD+, we confirmed that ADP-ribosylation occurs within apo-Ia-actin crystals soaked in mother liquor (Figure III-6A). On the other hand, within apo-Ia (E378S, E380A, and E380S)-actin crystals described in the next section, ADP-ribosylation assays showed no activity (Figure III-6A). In solution assays, the wild-type (WT) complex showed high activity, but ethylene glycol inhibited the ADP-ribosylation (Figure III-6B). Within the NAD+-Ia-actin structure, several ethylene glycol molecules were assigned in the structure. None of the ethylene glycol molecules

was around the NAD^+-binding site, so how they inhibit the reaction is not clear. Nonetheless, the structure of NAD^+-Ia-actin was obviously trapped in a prereaction state.

Ia has strong ART activity, but if actin is absent, it has weak NAD^+ glycohydrolase (NADase) activity[42,84]. The latter reaction is the ADP-ribosylation of water molecules and is indicative of the NAD^+ cleavage rate in the absence of actin. The EXE (Glu378 and Glu380) motif is important for the enzyme activity (Figure III-6A and Figure III-7A), and E380A and E380S mutations eliminated both NADase and ART activity. On the other hand, E378S blocked ART activity, but the enzyme retained about half its NADase activity, compared with WT. Using purified EXE motif mutants (E378S, E380A, and E380S), we solved the structures of the NAD^+-Ia (mutants)-actin complexes (Table III-2 and Figure III-7).

The overall crystal structure of NAD^+-Ia (mutant)-actin and the electron density of NAD^+ were similar to that of NAD^+-Ia (WT)-actin (Figure III-7). Not only the artificial structure of NAD^+-Ia (WT)-actin trapped in ethylene glycol but also structures of NAD^+-Ia (mutant)-actin revealed the nature of NAD^+ binding in the complex. It is noteworthy, however, that within the E380A structure, the position of the N-ribose in NAD^+ differs slightly from the others. This may explain how Glu380 strongly interacts with the 2' OH of N-ribose and plays an important role in nicotinamide cleavage activity.

Although the crystallization conditions and the protein packing of ßTAD-Ia-actin were basically the same as those of apo-Ia-actin, NAD^+-Ia-actin, and Ia-ADPR-actin (Figure III-3), large movements of three helices (H7, H8, and H9) were seen in theßTAD-Ia-actin structure that were not seen in the other structures (Figure III-8). As will be described in the following section, this movement appears to increase the strain on the NMN moiety and to induce a shift toward formation of an oxocarbenium cation. For that reason, we deem ßTAD-Ia-actin to be in the transition state SN1. With the exception of Arg177, the structure of the substrate actin molecule was unchanged in all of the structures, including ßTAD-Ia-actin.

III.3.2 Plasticity of the ARTT loop within the complex upon ADP-ribosylation

Successive structural analyses showed that the ARTT loop is the most flexible part of the Ia protein during the ADP-ribosylation reaction and that Tyr375 and Glu378 are present in at least two different states: the apo- and postreaction (ADP-ribosylated) state and the prereaction state (NAD^+-bound) (Figure III-3). Tyr375 is oriented inward, toward the toxin, in the apo- and postreaction state, but it is oriented toward the actin in the

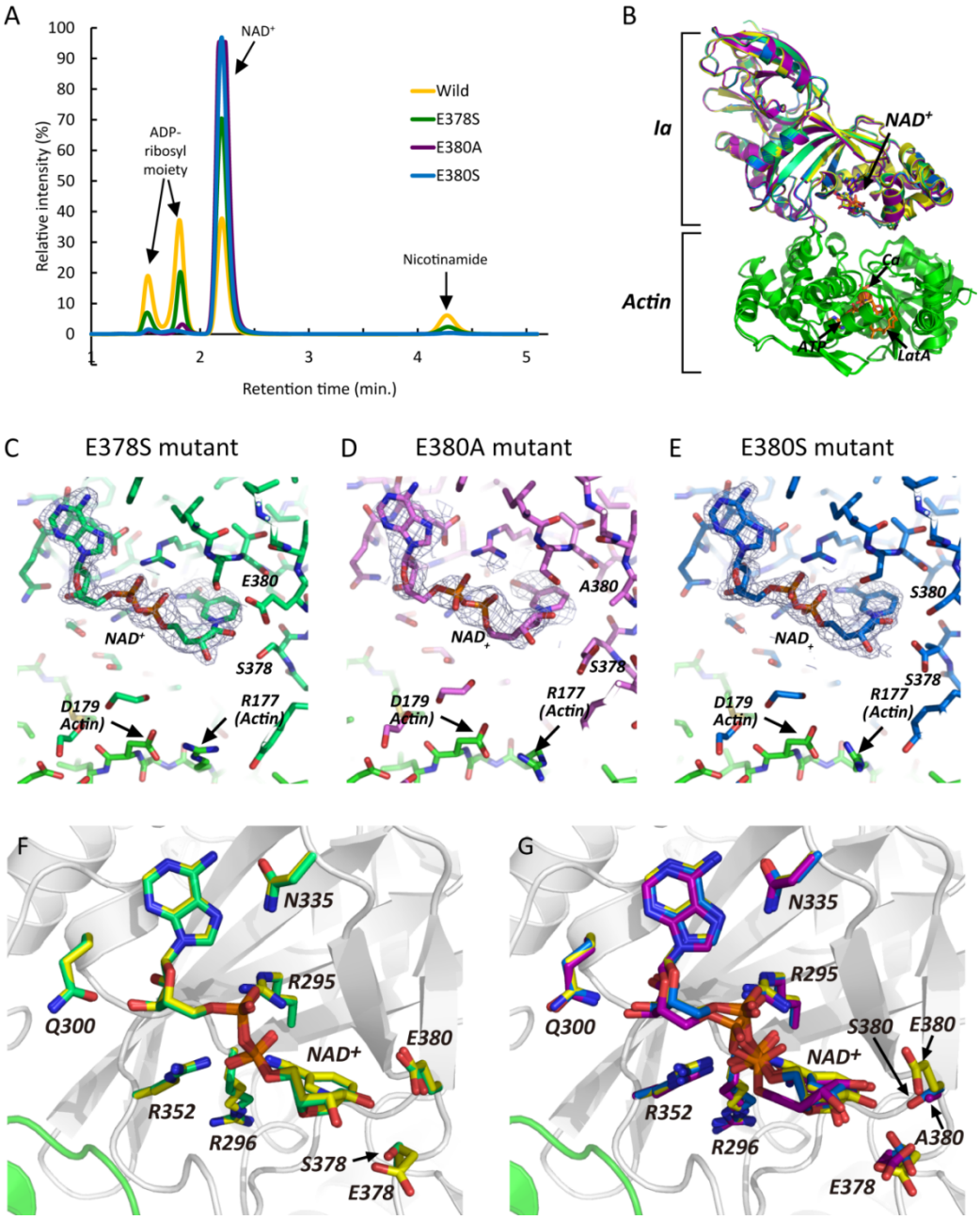

Figure III-7 A) NADase activities of Ia wild type and mutants measured by FPLC. Wild type (yellow), E378S (green), E380A (purple), and E380S (blue) are illustrated. The authentic ligands were analyzed alone, resulting in two peaks of 1.5 and 1.8 min for ADP -ribosyl moiety; 2.2-min peak is NAD^+, and 4.3-min peak is nicotinamide. B) Overall structures of four complexes of Ia in NAD^+-Ia (WT)-actin, NAD^+-Ia (E378S)-actin, NAD^+-Ia (E380A)-actin, and NAD^+-Ia (E380S)-actin. All of the complexes show NAD^+ bound in the prereaction state. C) Electron density around NAD^+ within the NAD^+-Ia (E378S)-actin, D) NAD^+-Ia (E380A)-actin, and E) NAD^+-Ia (E380S)-actin. All 2Fo-Fc electron density maps are at 1.0 σ. F) Comparison of WT vs. E378S mutant; wild type of Ia is in yellow and E378S mutant is in green. G) Comparison of WT vs. two E380 mutants. Wild type is in yellow, E380A mutant is in purple, and E380S mutant is in blue. All actins are in green. Y251, R295, R296, Q300, N335, R352, Y375, E378, and E380 are labeled in Ia.

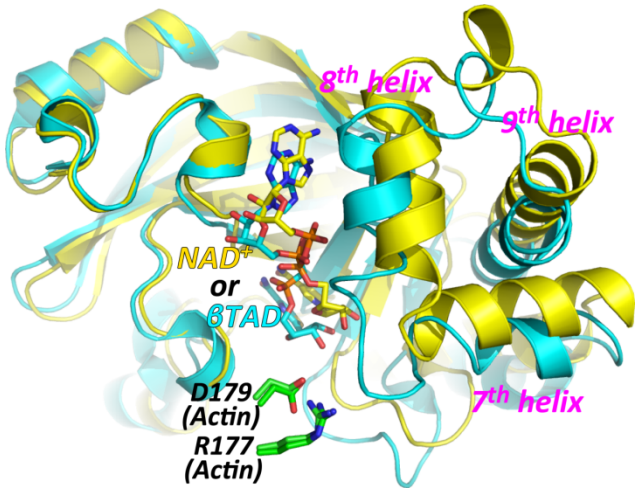

Figure III-8 Superposition of NAD+-Ia-actin (Ia: yellow) and βTAD-Ia-actin (Ia: cyan). Actin and other cofactors are depicted in the same color as the previous figures (Figure III-3). Two structures show similar conformation, except the seventh, eighth, and ninth helices (labeled in magenta) in the C-terminal domain of Ia.

prereaction state. On the other hand, Glu378 is in close proximity to the 2' OH and 3' OH of the N-ribose in NAD+-Ia-actin (NAD+-binding state), but it is oriented toward actin Arg177 in the apo- and postreaction state. This plasticity of Glu378 is totally different from Glu380, which remains in the same position throughout the reaction. Within the motif, Tyr375 is at the first turn of the ARTT loop, and it was suggested that Tyr375 plays an important role in the recognition of the target protein[46]. In the prereaction state, the observed interaction between Tyr375 and actin could serve to stabilize the NAD+-Ia-actin triple complex, but the weak electron density of Tyr375 suggests that the interaction is not very strong. In the second turn of the ARTT loop, Glu378 may be important for recognition of actin Arg177 residue. Experimentally, Glu378 was shown to be essential for both the NADase and ART activities[42]. Upon ADP ribosylation, the observed movement of Glu378 (from the apo-reaction state to the prereaction state and from the prereaction to the postreaction state) appears to correlate with the rotation of the N-ribose and explains why Glu378 has dual activity: in the prereaction state, Glu378 acts with Glu380 to induce nicotinamide cleavage and is also important for keeping the oxocarbenium cation from reacting with unfavorable water during the transition from the prereaction to the postreaction state. Another ART, *C. botulinum* C3, alters cytoskeletal signaling by selectively modifying the low-molecular-mass GTP-binding protein RhoA at Asn41. Although Ia and C3 ADP-ribosylate different substrates, they have a strong structural similarity, which suggests that they have a similar substrate amino acid recognition mechanism[41,46], especially with respect to the ARTT loop. The importance of the ARTT loop in C3 and its plasticity has been discussed elsewhere[85], but the present study sheds light on the role of ARTT plasticity in ADP ribosylation within

the structure of the ART-substrate protein complex.

I.3.3 Reaction mechanism inferred from the structures

The mechanism by which an SN1 reaction leads to ADP-ribosylation of Arg177 was suggested by studies of the Ia structure and its site-directed mutagenesis[42]. The positively charged Arg295 and Arg352 (Ia) interact electrostatically with NAD^+ phosphate and contribute to the highly folded and strained conformation of the NMN ring-like conformation. This specific structure of NAD^+ is conserved among all ART family members. The specific conformation appears to induce an equilibrium shift toward formation of an oxocarbenium cation. After cleavage of the nicotinamide, the oxocarbenium cation may be stabilized via Tyr251 through a cation-π interaction[86]. In the present NAD+-Ia-actin structure, the distance between the nucleophile (Arg177) and the electrophile (NC1 of N-ribose) is 8.2 Å, making it necessary to reduce the distance between Arg177 and NC1 of N-ribose. In an earlier paper, we proposed a strain-alleviation model in which a second oxocarbenium ion acts as an intermediary[52]. In that model, strain" referred to the highly folded and strained conformation of NMN, whereas "alleviation" referred to the rotation of the N-ribose after scission of the nicotinamide. That is, SN1 cleavage produced the first oxocarbenium cation, after which rotation occurred via NP-NO5 of ADP-ribose to produce a second cationic intermediate, which enabled NC1 of N-ribose to approach the guanidyl nitrogen of Arg177. In the present pre- and postreaction state structural study, the strain-alleviation model was confirmed experimentally and was improved. The key features of the improved model are as follows (Figure III-9AB); (1) The ADP moiety is gripped by Ia, and then the ADP-ribosylation reaction occurs. The grip is necessary for the subsequent rotation (2). To reduce the distance between the nucleophile (Arg177) and the electrophile (NC1 of N-ribose), after the first oxocarbenium ion intermediate is produced (SN1 reaction), the rotation of N-ribose occurs mainly via rotation of both O3-NP and NP-NO5 (3). The present structure confirms that the N-ribose 3' OH is in close proximity to Asp179 (3.5 Å) within Ia-ADPR-actin. We envision that actin Asp179 plays a stabilizing role by making contact with the N-ribose (4). Arg177 tilts slightly to react with N-ribose.

The successive structures of each reaction step are shown in Figure III-9C: the apo-state, the prereaction state, βTAD-Ia-actin as a transition state in the SN1 reaction, and the postreaction state. We speculate that the observed movement of the helices in βTAD-Ia-actin increases the strain on the nicotinamide of NAD^+ so that it proceeds to the first SN1 cleavage efficiently. In summary, a simple strain-alleviation model can explain arginine ADP-ribosylation occurring via two oxocarbenium ion intermediates.

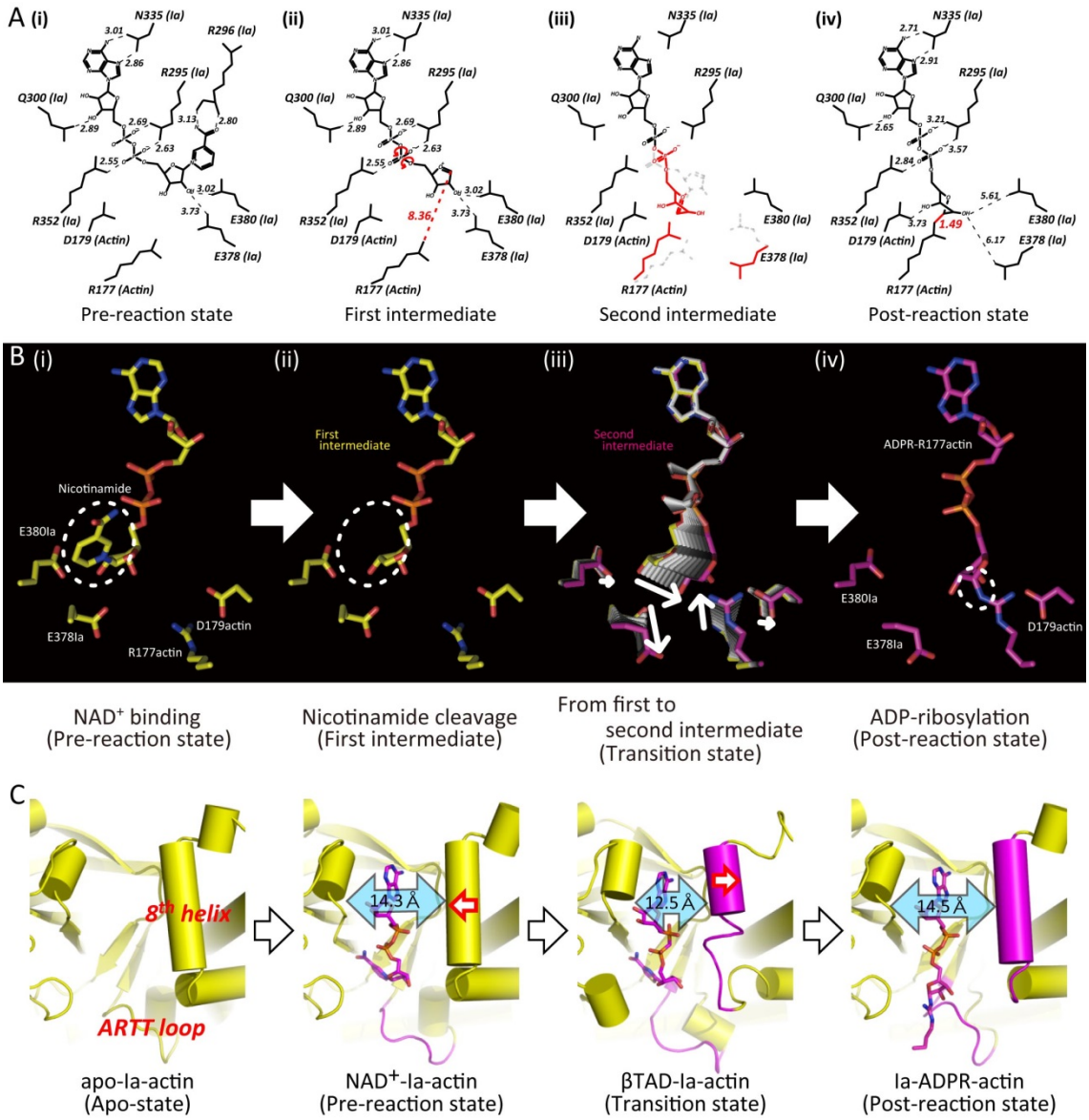

Figure III-9 Schematic illustrating the mechanism of ADP-ribosylation. A) SN1 mechanism in Ia: (i) NAD+-Ia-Actin as the prereaction state; (ii) nicotinamide cleavage occurs via an SN1 reaction induced by an NMN ring-like structure and the first oxocarbenium cation intermediate is formed with a strained conformation; (iii) the second cationic intermediate is induced through alleviation of the strained conformation mainly by O3-NP and NP-NO5 rotation, and then NC1 of N-ribose nucleophilically attacks Arg177 of actin; (iv) Ia-ADPR-actin as the postreaction state. B) Cartoon representation of panel A. C) Successive structures during ADP-ribosylation and the structure of each reaction: step 1 (apo-Ia-actin), step 2 [NAD+-Ia-actin (prereaction state)], step 3 [βTAD-Ia-actin (transition state)], and step 4 [Ia-ADPR-actin (postreaction state)].

III.4 Discussion

We report the structure of the NAD+-Ia-actin and Ia-ADPR-actin complexes, providing insight into the reaction mechanism of ADP-ribosylation. Arginine ADP-ribosylation is a modification catalyzed by both bacterial toxins and human membrane-associated ARTs. The trapped ADPR structure will provide important information about the reaction

mechanism underlying ADP ribosylation of arginine. Margarit et al. reported the crystal structures of SpvB-modified ADPR-actin[45]. However, their ADPR-actin structure did not include SpvB, so the modified residue was not visible due to the plasticity of the complex. Our structure of ADPR-arginine was trapped because Ia gripped the ADP moiety of ADP-ribosylated arginine. As mentioned above, we were unable to obtain NAD^+ cocrystals because Ia and actin separate after ADP ribosylation. However, NAD^+ soaking worked well because Ia-ADP-ribosylated-actin was retained within the crystal packing. Given that the structure of SpvB-modified ADPR-actin does not change from unmodified G-actin, the mechanism of inhibition of actin polymerization is thought to occur primarily through steric disruption of intrafilament contacts by the ADP-ribosylated Arg177[45,87].

Within the crystal structure of Ia-ADPR-actin, the ADP-ribosyl moiety was observed, but in solution without toxin, the flexible ADP-ribosyl moiety was situated near Arg177, where it disrupted actin-actin contacts and thereby inhibited actin polymerization. As described before[50], the NMN moieties of all ARTs bind in a similar compact fashion. On the other hand, the AMP moiety shows variation. Remarkably, the adenine ribose is oriented differently in type II *diphtheria* toxin group. Recently, the conformational analysis of NAD^+ was reported[88]. The conformation is different in NAD^+ bound to redox enzyme and nonredox enzyme. A specific feature of ARTs is a small ChiN value that is never seen in redox NAD. Actually, the ChiN torsion angle of NAD^+-Ia-actin is 3.1° (ChiA = −115°, GammaA = 53.2°, and ZetaA = −158.0°). Although NAD^+ had been postulated to strain the N-glycosidic bond, NAD^+ with different ChiN values was found to exhibit similar C1D-N1N bond cleavage barriers in water. As a next step, however, we need to evaluate the bond barriers, including supporting amino acids near NMN not in water. Two glutamates (378 and 380 in Ia) are especially important for the catalysis. The bond cleavage is determined not only by the physical property of the specific conformation of NAD^+ but also by a chemical factor. Also, our strain and alleviation model is an important description of the trigger of conformational change after cleavage of nicotinamide. There should be

Table III-3 Residue–residue interaction between Ia and actin (3.5Å cutoff)

Ia	-	Actin	Distance (Å)	Interaction
Y60	-	E276	2.61	Ionic bond
Y60	-	N280	3.24	Hydrogen bond
D61	-	K284	3.16	Ionic bond
Y62	-	N280	2.61	Hydrogen bond
Y311	-	E270	2.58	Ionic bond
S347	-	M176	3.35	Hydrogen bond
S347	-	S271	3.39	Hydrogen bond
S347	-	N280	2.84	Hydrogen bond
K351	-	E270	2.89	Ionic bond
K351	-	E276	2.78	Ionic bond
R352	-	E270	3.39	Ionic bond

Table III-4 Properties of residues

Residue		Glu378	Glu380	Tyr375
Activities by mutational study*	NADase	↓	↓ ↓ ↓	N.D.
	ARTase	↓ ↓ ↓	↓ ↓ ↓	N.D.
Distance from NAD^+**		++ (N-ribose)	++ (N-ribose)	–
Nicotinamide cleavage (I) or Transferase (II)		I, II	I	II
Related conformation		NMN ring-like conformation	NMN ring-like conformation	
Role and Comment		It is conserved and flexible residue on ARTT loop. After nicotinamide clevage, this residue may make N-ribose rotation. It may recognize of Arg177 of actin, but it was not trapped in our static structure.	It is conserved and rigid residue on ARTT loop. This is essential for formation of NMN ring-like conformation.	It is conserved Y/F and flexible residue on ARTT loop. This residue seems to be important with substrate protein (actin) recognition.

Residue		Ser338	Phe349	
Activities by mutational study*	NADase	↓ ↓ ↓	↓ ↓ ↓ (Ala)	No decrease (Tyr)
	ARTase	↓ ↓ ↓	↓ ↓ ↓ (Ala)	↓ ↓ (Tyr)
Distance from NAD^+**		+ (Nicotinamide)	+ (Nicotinamide)	
Nicotinamide cleavage (I) or Transferase (II)		I	I	
Related conformation		Scorpion shape head***	Scorpion shape tail***	
Role and Comment		These residues are STS motif and Ser338 fix nicotinamide as head part of scorpion structure.	This residue, as tip of scorpion tail,may fix nicotinamide.	

Residue		Tyr251	Arg295	Arg296 (main chain)
Activities by mutational study*	NADase	↓ ↓ ↓	↓ ↓ ↓	N.D.
	ARTase	↓ ↓ ↓	↓ ↓ ↓	N.D.
Distance from NAD^+**		++ (N-ribose)	++ (N-phosphate)	++ (Nicotinamide)
Nicotinamide cleavage (I) or Transferase (II)		I, II	I, II	I
Related conformation		NMN ring-like conformation	NMN ring-like conformation	NMN ring-like conformation
Role and Comment		This may be related to nicotinamide cleavage and transferace activity via making cation- π interaction with N-ribose.	ADP moiety gripping.	ADP moiety gripping

Residue		Gln300	Asn335	Arg352
Activities by mutational study*	NADase	N.D.	N.D.	↓ ↓ ↓
	ARTase	N.D.	N.D.	↓ ↓ ↓
Distance from NAD^+**		++ (A-ribose)	++ (Adenine)	++ (A-phosphate)
Nicotinamide cleavage (I) or Transferase (II)		I, II	I, II	I, II
Related conformation				NMN ring-like conformation
Role and Comment		ADP moiety gripping	ADP moiety gripping	ADP moiety gripping

* Mutational study referred to Nagahama et al., J. Bacteriol (2000) and our previous report Tsuge et al., JMB (2003).
* Arrows indicate decreased degree of enzyme activity upon single mutaion to alanine and N.D. means Not Determined. ↓ ↓ ↓ means almost diminished.
** Distances cut off with "++" within 4 Å, "+" from 4 to 6 Å and "-" over 6Å
***This conformation is referred to Lee et al., J. Med. Chem. (2010)

equilibrium between NAD+ and oxocarbenium cation/nicotinamide. If there is still strain in the first oxocarbenium cation intermediate, it creates the second conformation of the oxocarbenium cation intermediate by alleviation and finally interacts with arginine. It seems that the strain strongly supports the forward reaction not to go backward. Finally, we summarized the residue-residue interactions between Ia and actin and the properties of the key residues (Tables III-3 and III-4).

Another available structure of an ART-substrate complex is that of exotoxin A-elongation factor 2 (ETA-EF2). With ETA, the modified residue is not arginine but diphthamide (a modified histidine)[51,89]. Jørgensen et al. reported that the diphthamide N3 nucleophilic atom remains about 10 Å from the electrophilic C1 center of the N-ribose within the complex; consequently, one additional step is necessary for consummation of the nucleophilic substitution reaction[51]. They proposed a model in which the EF2 loop, which includes the diphthamide residue, migrates toward the N-ribose. If this does occur, a similar strain-alleviation model may also explain the ADP-ribosylation reaction: the L1 and L3 loops of ETA grip the ADP until the N-ribose rotates to react with the diphthamide N3 after scission of the nicotinamide (Figure III-10). They also showed that a substrate acidic residue is important and that Asp696 forms a hydrogen bond with the N-ribose 2' OH within ADPR-eEF2, and they suggested that an Asp696 analog likely

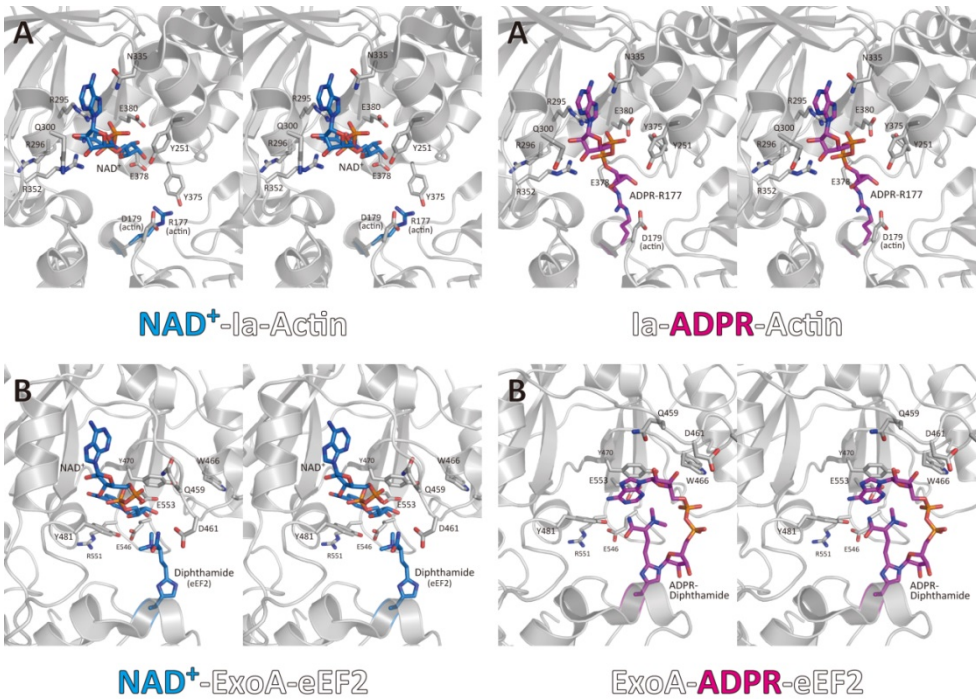

Figure III-10 Comparison of ARTC and ARTD complexes and reactions. A) The structure of the A) NAD+-Ia-actin and Ia-ADPR-actin complexes are compared with B) NAD+-ExoA-eEF2 and ExoA-ADPR-eEF2 in stereo view. NAD+, Arg177 of actin and Diphthamide of eEF2 are depicted in blue. ADP-ribosylated Arg177 and diphthamide are in magenta.

interacts with the N-ribose hydroxyl group during or after the arginine ADP-ribosylation of Gα's and actin[51]. Given the βTAD-Ia-actin structure, we previously suggested that actin Asp179 serves that function and forms a hydrogen bond with N-ribose[52]. In the present study, we confirmed this to be true within the Ia-ADPR-actin structure. Our strain and alleviation model is compared with the old model as mentioned in previous report[52].

ADP-ribosyl transferases have been identified not only in bacteria but also in eukaryotic cells. Recently, a classification was proposed based on the key sequence similarity among all ARTs, including nonbacterial ARTs[90,91]. Within this scheme, ARTs are classified into two large groups as Figure III-1: ARTC (R-S-E group: C2I, Ia and C3) and ARTD (H-Y-E group: diphtheria toxin group)[90]. Mammalian and avian ARTs, which are known to regulate a variety of important cell functions, including immune responses, cell adhesion, cell signaling, and metabolism[92], belong to the ARTC group. Poly-ADP-ribosyl transferases act as sensors of DNA strand breaks and catalyze poly-ADP-ribosylation of themselves and various target proteins[93]. Poly-ADP-ribosyl transferases belong to the ARTD group. Although the target proteins and the residues modified by these ARTs differ, their basic core structural similarity, the structural similarity of the strained conformations of NAD^+, and the common acidic residue in the substrate protein needed to fix the N-ribose suggest that all ARTs make use of a common reaction mechanism. The high-resolution structure and simple reaction mechanism reported here will provide an understanding of the reaction. Finally, the unique complex structure also provides valuable information needed to design inhibitors of ART family proteins[94].

Actin is one the most abundant and well-conserved proteins in cells and is involved in such important cellular functions as cell motility, contractility, intracellular transport, and the control of cell shape and polarity[95]. Actin exists in two forms as the major component of the cytoskeleton, a monomeric form (G-actin) and a filamentous form (F-actin) (Figure III-11A). The structures of actin after ADP-ribosylation by SpvB have been reported[45]. It is of interest whether this modification induces conformational changes in actin that are incompatible with filament formation, and whether the presence of ADPR at Arg177 causes a steric clash preventing the protein-protein interactions necessary for polymerization (Figure III-11B). The reported structure of ADPR-actin shows that ADP-ribosylation by SpvB induces no substantial conformational alterations in actin, though the ADP-ribosylation was not trapped crystallographically in the structure because of its flexibility[45]. Those investigators concluded that a model in which steric clash hinders intraprotomer contacts within the filament provides the most likely explanation for the activity of SpvB. The first visible structure of ADP-ribosylated

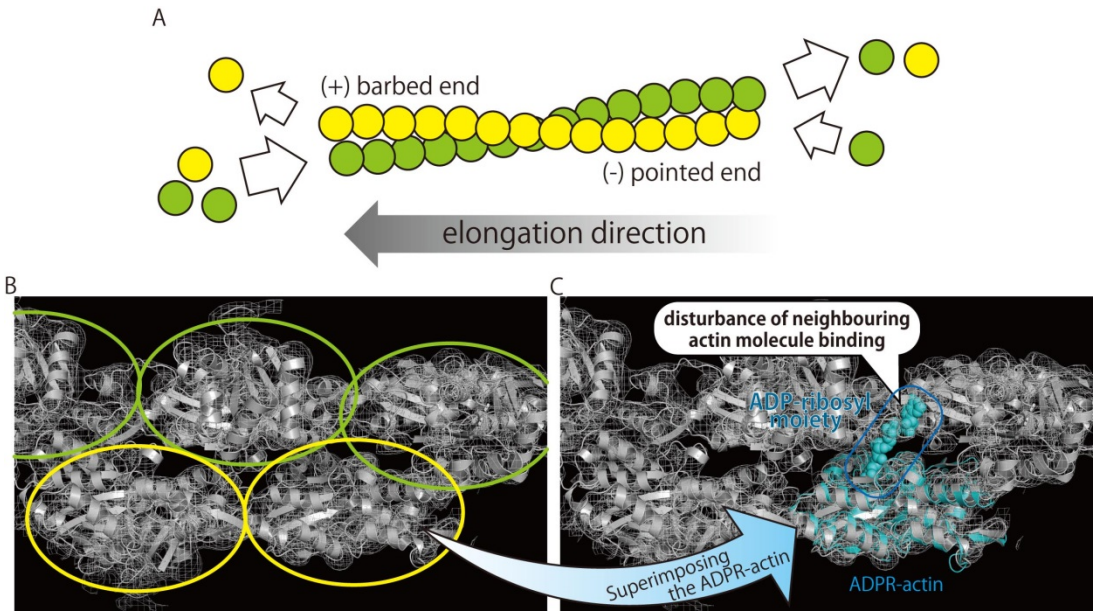

Figure III-11 Fitting of ADP-ribosylated actin into the filamentous actin structure. A) Actin filaments undergo treadmilling. Actin monomers add at the (+) barbed end and dissociate from the (-) pointed end. B) In left panel, the structure of intact actin (yellow ang green circles) and ADPR-actin (4H0T, magenta) were superposed into the cryo-microscopy electron density map (EMD-5168). Right panel: Closeup view of ADPR-actin in the electron density.

actin, within the Ia-ADPR-actin complex, confirmed the earlier finding that actin is unchanged by ADP-ribosylation. Recently the high-resolution structure of F-actin was revealed using cryo-electron microscopy[96,97]. We superimposed the ADPR-actin monomer on the filamentous actin structure using a UCSF chimera[98] (Figure III-11B). This model also supports that ADP-ribosylation prevents actin polymerization through steric clash.

Conclusions

The study was undertaken for obtain insights into TNF-α inducing mechanism for tumor necrosis factor α inducing protein (Tipα) from *Helicobacter Pylori*, transcription mechanism for PB2 subunit of RNA polymerase from Influenza A virus (H1N1) and reaction mechanism for toxic subunit of Iota toxin from *Clostridium perfringens*. All results will be the clue to design drugs against each protein.

In Chapter I, we revealed the crystal structure of deletion mutant of TNF-α inducing protein, Tipα, at 2.47 Å. This structure showed that the two monomers are linked through electrostatic and hydrophobic interactions at the flexible N-terminal region. This structural feature of del-Tipα suggests that the structure and oligomerization state of Tipα is maintained by the disulfide bridge linking the N-terminal portions of the molecules. CD spectra in both the near-UV and far-UV regions showed that Tipα and del-Tipα have the same pattern of rotational strength, which suggests that the solution structures of Tipα and del-Tipα are the same, despite the fact that Tipα contains disulfide bonds and del-Tipα does not. Furthermore, we obtained the structure, which is open jaw of Tipα, and preliminary X-ray small angle scattering analysis revealed that Tipα dimer forms open jaw at basic and closed jaw at acidic condition in solution. These results suggested that conformation of dimer depends on pH.

In Chapter II, we report the crystal structure of the middle domain of PB2 with or without m^7GTP at 1.7 Å and 2.0 Å resolution, respectively, in the same crystalline with H1N1 type for the first time. We prepared the PB2 middle domain with two mutations (P453H, I471T) to increase electrostatic potential and solubility. Interestingly, the m^7GTP in our structure has unique conformation that is different from the reported structure with H3N2 type. 7-Methyl-guanine is fixed in the pocket, but particularly significant changes are seen in ribose and tri-phosphate region. From the results of preliminary X-ray analysis of GTP analogs, methylated group is necessary for substrate recognition. These results may be a key to reveal how PB2 subunit capture a host mRNA and how to inhibit it to prevent transcription of influenza RNA.

In Chapter III, we reported high-resolution structures of NAD^+-Ia-actin and Ia-ADPR-actin obtained by soaking apo-Ia-actin crystal with NAD^+ under different conditions. We found that ethylene glycol as cryo-protectant inhibits ADP-ribosylation. Then, under one soaking condition with ethylene glycol, successfully captured NAD^+

binding Ia-actin complex in crystal. Under another soaking condition, we obtained ADP-ribosylated actin complexed with Ia. According to these structures, we revealed the strain-alleviation model as ADP-ribosylation mechanism in ARTC group. Furthermore we visualized ADP-ribosylated actin fully and then, we could show the model, using model of filamentous actin, which ADP-ribosylation prevents actin polymerization through steric clash. We suggest that this mechanism may be applied to other ADP-ribosyltransferases belonging to ARTC group. We also suggest that our soaking method will be available for other enzyme substrate-protein complex.

References

1. Ogata, S., Kamiya, S. (ed.) *Microbiology・Immunology*, (IGAKUHYORONSHA, INC., Tokyo, 2002).
2. Yoshioka, Y. (ed.) *Uirusu・Saikin to Kansensyo ga wakaruhon*, (YODOSHA CO .,LTD., Tokyo, 2004).
3. Correa, P. Helicobacter pylori infection and gastric cancer. *Cancer Epidemiol Biomarkers Prev* **12**, 238s-241s (2003).
4. Peek, R.M., Jr. & Blaser, M.J. Helicobacter pylori and gastrointestinal tract adenocarcinomas. *Nat Rev Cancer* **2**, 28-37 (2002).
5. Group, I.W. Schistosomes, liver flukes and Helicobacter pylori. IARC Working Group on the Evaluation of Carcinogenic Risks to Humans. Lyon, 7-14 June 1994. *IARC Monogr Eval Carcinog Risks Hum* **61**, 1-241 (1994).
6. Covacci, A. et al. Molecular characterization of the 128-kDa immunodominant antigen of Helicobacter pylori associated with cytotoxicity and duodenal ulcer. *Proc Natl Acad Sci U S A* **90**, 5791-5 (1993).
7. Nilsson, C. et al. Correlation between cag pathogenicity island composition and Helicobacter pylori-associated gastroduodenal disease. *Infect Immun* **71**, 6573-81 (2003).
8. Normark, S., Nilsson, C., Normark, B.H. & Hornef, M.W. Persistent infection with Helicobacter pylori and the development of gastric cancer. *Adv Cancer Res* **90**, 63-89 (2003).
9. Phadnis, S.H., Ilver, D., Janzon, L., Normark, S. & Westblom, T.U. Pathological significance and molecular characterization of the vacuolating toxin gene of Helicobacter pylori. *Infect Immun* **62**, 1557-65 (1994).
10. Suganuma, M. et al. TNF-alpha-inducing protein, a carcinogenic factor secreted from H. pylori, enters gastric cancer cells. *Int J Cancer* **123**, 117-22 (2008).
11. Park, S.M. et al. Infection with Helicobacter pylori expressing the cagA gene is not associated with an increased risk of developing peptic ulcer diseases in Korean patients. *Scand J Gastroenterol* **33**, 923-7 (1998).
12. Shimoyama, T. et al. High prevalence of the CagA-positive Helicobacter pylori strains in Japanese asymptomatic patients and gastric cancer patients. *Scand J Gastroenterol* **32**, 465-8 (1997).
13. Moore, R.J. et al. Mice deficient in tumor necrosis factor-alpha are resistant to skin carcinogenesis. *Nat Med* **5**, 828-31 (1999).
14. Suganuma, M. et al. Essential role of tumor necrosis factor alpha (TNF-alpha) in tumor promotion as revealed by TNF-alpha-deficient mice. *Cancer Res* **59**, 4516-8 (1999).
15. Suganuma, M. et al. New tumor necrosis factor-alpha-inducing protein released from Helicobacter pylori for gastric cancer progression. *J Cancer Res Clin Oncol* **131**, 305-13 (2005).
16. Kuzuhara, T., Suganuma, M., Kurusu, M. & Fujiki, H. Helicobacter pylori-secreting protein Tipalpha is a potent inducer of chemokine gene expressions in stomach cancer cells. *J Cancer Res Clin Oncol* **133**, 287-96 (2007).
17. Suganuma, M., Kuzuhara, T., Yamaguchi, K. & Fujiki, H. Carcinogenic role of tumor necrosis factor-alpha inducing protein of Helicobacter pylori in human stomach. *J Biochem Mol Biol* **39**, 1-8 (2006).
18. Kuzuhara, T., Suganuma, M., Oka, K. & Fujiki, H. DNA-binding activity of TNF-alpha inducing protein from Helicobacter pylori. *Biochem Biophys Res Commun* **362**, 805-10 (2007).

19. Reid, A.H., Taubenberger, J.K. & Fanning, T.G. The 1918 Spanish influenza: integrating history and biology. *Microbes Infect* **3**, 81-7 (2001).
20. Elton, D., Digard, P., Tiley, L. & Ortin, J. Structure and function of the influenza virus RNP. in *In Current Topics in Influenza Virology* (ed. Kawaoka, Y.) (Horizon Scientific,Norfork, 2005).
21. Plotch, S.J., Bouloy, M., Ulmanen, I. & Krug, R.M. A unique cap(m7GpppXm)-dependent influenza virion endonuclease cleaves capped RNAs to generate the primers that initiate viral RNA transcription. *Cell* **23**, 847-58 (1981).
22. Mukaigawa, J. & Nayak, D.P. Two signals mediate nuclear localization of influenza virus (A/WSN/33) polymerase basic protein 2. *J Virol* **65**, 245-53 (1991).
23. Hatta, M., Gao, P., Halfmann, P. & Kawaoka, Y. Molecular basis for high virulence of Hong Kong H5N1 influenza A viruses. *Science* **293**, 1840-2 (2001).
24. Steel, J., Lowen, A.C., Mubareka, S. & Palese, P. Transmission of influenza virus in a mammalian host is increased by PB2 amino acids 627K or 627E/701N. *PLoS Pathog* **5**, e1000252 (2009).
25. Subbarao, E.K., Kawaoka, Y. & Murphy, B.R. Rescue of an influenza A virus wild-type PB2 gene and a mutant derivative bearing a site-specific temperature-sensitive and attenuating mutation. *J Virol* **67**, 7223-8 (1993).
26. Kuzuhara, T. et al. Structural basis of the influenza A virus RNA polymerase PB2 RNA-binding domain containing the pathogenicity-determinant lysine 627 residue. *J Biol Chem* **284**, 6855-60 (2009).
27. Tarendeau, F. et al. Host determinant residue lysine 627 lies on the surface of a discrete, folded domain of influenza virus polymerase PB2 subunit. *PLoS Pathog* **4**, e1000136 (2008).
28. Ueda, K. & Hayaishi, O. ADP-ribosylation. *Annu Rev Biochem* **54**, 73-100 (1985).
29. Gill, D.M., Pappenheimer, A.M., Jr., Brown, R. & Kurnick, J.T. Studies on the mode of action of diphtheria toxin. VII. Toxin-stimulated hydrolysis of nicotinamide adenine dinucleotide in mammalian cell extracts. *J Exp Med* **129**, 1-21 (1969).
30. Gill, D.M. & Meren, R. ADP-ribosylation of membrane proteins catalyzed by cholera toxin: basis of the activation of adenylate cyclase. *Proc Natl Acad Sci U S A* **75**, 3050-4 (1978).
31. Moss, J. & Vaughan, M. Mechanism of action of choleragen. Evidence for ADP-ribosyltransferase activity with arginine as an acceptor. *J Biol Chem* **252**, 2455-7 (1977).
32. Katada, T. & Ui, M. Direct modification of the membrane adenylate cyclase system by islet-activating protein due to ADP-ribosylation of a membrane protein. *Proc Natl Acad Sci U S A* **79**, 3129-33 (1982).
33. Moss, J., Garrison, S., Oppenheimer, N.J. & Richardson, S.H. NAD-dependent ADP-ribosylation of arginine and proteins by Escherichia coli heat-labile enterotoxin. *J Biol Chem* **254**, 6270-2 (1979).
34. Van Ness, B.G., Howard, J.B. & Bodley, J.W. ADP-ribosylation of elongation factor 2 by diphtheria toxin. Isolation and properties of the novel ribosyl-amino acid and its hydrolysis products. *J Biol Chem* **255**, 10717-20 (1980).
35. Aktories, K., Weller, U. & Chhatwal, G.S. Clostridium botulinum type C produces a novel ADP-ribosyltransferase distinct from botulinum C2 toxin. *FEBS Lett* **212**, 109-13 (1987).
36. Aktories, K. et al. Botulinum C2 toxin ADP-ribosylates actin. *Nature* **322**, 390-2 (1986).
37. Vandekerckhove, J., Schering, B., Barmann, M. & Aktories, K. Clostridium perfringens iota toxin ADP-ribosylates skeletal muscle actin in Arg-177. *FEBS Lett* **225**, 48-52 (1987).
38. Lang, A.E. et al. Photorhabdus luminescens toxins ADP-ribosylate actin and RhoA to force actin clustering. *Science* **327**, 1139-42 (2010).
39. Aktories, K., Lang, A.E., Schwan, C. & Mannherz, H.G. Actin as target for modification by bacterial protein toxins. *FEBS J* **278**, 4526-43 (2011).

40. Aktories, K. & Wegner, A. Mechanisms of the cytopathic action of actin-ADP-ribosylating toxins. *Mol Microbiol* **6**, 2905-8 (1992).
41. Han, S., Craig, J.A., Putnam, C.D., Carozzi, N.B. & Tainer, J.A. Evolution and mechanism from structures of an ADP-ribosylating toxin and NAD complex. *Nat Struct Biol* **6**, 932-6 (1999).
42. Tsuge, H. et al. Crystal structure and site-directed mutagenesis of enzymatic components from Clostridium perfringens iota-toxin. *J Mol Biol* **325**, 471-83 (2003).
43. Schleberger, C., Hochmann, H., Barth, H., Aktories, K. & Schulz, G.E. Structure and action of the binary C2 toxin from Clostridium botulinum. *J Mol Biol* **364**, 705-15 (2006).
44. Sundriyal, A., Roberts, A.K., Shone, C.C. & Acharya, K.R. Structural basis for substrate recognition in the enzymatic component of ADP-ribosyltransferase toxin CDTa from Clostridium difficile. *J Biol Chem* **284**, 28713-9 (2009).
45. Margarit, S.M., Davidson, W., Frego, L. & Stebbins, C.E. A steric antagonism of actin polymerization by a salmonella virulence protein. *Structure* **14**, 1219-29 (2006).
46. Han, S., Arvai, A.S., Clancy, S.B. & Tainer, J.A. Crystal structure and novel recognition motif of rho ADP-ribosylating C3 exoenzyme from Clostridium botulinum: structural insights for recognition specificity and catalysis. *J Mol Biol* **305**, 95-107 (2001).
47. Menetrey, J. et al. NAD binding induces conformational changes in Rho ADP-ribosylating clostridium botulinum C3 exoenzyme. *J Biol Chem* **277**, 30950-7 (2002).
48. Evans, H.R. et al. The crystal structure of C3stau2 from Staphylococcus aureus and its complex with NAD. *J Biol Chem* **278**, 45924-30 (2003).
49. Vogelsgesang, M., Stieglitz, B., Herrmann, C., Pautsch, A. & Aktories, K. Crystal structure of the Clostridium limosum C3 exoenzyme. *FEBS Lett* **582**, 1032-6 (2008).
50. O'Neal, C.J., Jobling, M.G., Holmes, R.K. & Hol, W.G. Structural basis for the activation of cholera toxin by human ARF6-GTP. *Science* **309**, 1093-6 (2005).
51. Jorgensen, R. et al. Exotoxin A-eEF2 complex structure indicates ADP ribosylation by ribosome mimicry. *Nature* **436**, 979-84 (2005).
52. Tsuge, H. et al. Structural basis of actin recognition and arginine ADP-ribosylation by Clostridium perfringens iota-toxin. *Proc Natl Acad Sci U S A* **105**, 7399-404 (2008).
53. Tosi, T., Cioci, G., Jouravleva, K., Dian, C. & Terradot, L. Structures of the tumor necrosis factor alpha inducing protein Tipalpha: a novel virulence factor from Helicobacter pylori. *FEBS Lett* **583**, 1581-5 (2009).
54. Jang, J.Y. et al. Crystal structure of the TNF-alpha-Inducing protein (Tipalpha) from Helicobacter pylori: Insights into Its DNA-binding activity. *J Mol Biol* **392**, 191-7 (2009).
55. Gao, M. et al. Crystal structure of TNF-alpha-inducing protein from Helicobacter pylori in active form reveals the intrinsic molecular flexibility for unique DNA-binding. *PLoS One* **7**, e41871 (2012).
56. Otwinowski, Z. & Minor, W. *Processing of X-ray Diffraction Data Collected in Oscillation Mode*, (Academic Press, New York, 1997).
57. suite, T.C. The CCP4 suite: programs for protein crystallography. *Acta Crystallogr D Biol Crystallogr* **50**, 760-3 (1994).
58. Terwilliger, T. SOLVE and RESOLVE: automated structure solution, density modification and model building. *J Synchrotron Radiat* **11**, 49-52 (2004).
59. McRee, D.E. XtalView/Xfit--A versatile program for manipulating atomic coordinates and electron density. *J Struct Biol* **125**, 156-65 (1999).
60. Laskowski, R.A., Rullmannn, J.A., MacArthur, M.W., Kaptein, R. & Thornton, J.M. AQUA and PROCHECK-NMR: programs for checking the quality of protein structures solved by NMR. *J Biomol NMR* **8**, 477-86 (1996).
61. Combet, C., Jambon, M., Deleage, G. & Geourjon, C. Geno3D: automatic

comparative molecular modelling of protein. *Bioinformatics* **18**, 213-4 (2002).
62. Holm, L. & Sander, C. Dali: a network tool for protein structure comparison. *Trends Biochem Sci* **20**, 478-80 (1995).
63. Bieger, B., Essen, L.O. & Oesterhelt, D. Crystal structure of halophilic dodecin: a novel, dodecameric flavin binding protein from Halobacterium salinarum. *Structure* **11**, 375-85 (2003).
64. Kuzuhara, T., Suganuma, M., Tsuge, H. & Fujiki, H. Presence of a motif conserved between Helicobacter pylori TNF-alpha inducing protein (Tipalpha) and penicillin-binding proteins. *Biol Pharm Bull* **28**, 2133-7 (2005).
65. Yoshida, M. et al. Cloning and characterization of a novel membrane-associated antigenic protein of Helicobacter pylori. *Infect Immun* **67**, 286-93 (1999).
66. Liu, Y., Meng, G., Luo, M. & Zheng, X. Crystallization and X-ray crystallographic analysis of the cap-binding domain of influenza A virus H1N1 polymerase subunit PB2. *Acta Crystallogr Sect F Struct Biol Cryst Commun* **69**, 280-3 (2013).
67. Guilligay, D. et al. The structural basis for cap binding by influenza virus polymerase subunit PB2. *Nat Struct Mol Biol* **15**, 500-6 (2008).
68. Liu, Y. et al. Structural and functional characterization of K339T substitution identified in the PB2 subunit cap-binding pocket of influenza A virus. *J Biol Chem* **288**, 11013-23 (2013).
69. Vagin, A. & Teplyakov, A. Molecular replacement with MOLREP. *Acta Crystallogr D Biol Crystallogr* **66**, 22-5 (2010).
70. Afonine, P.V. et al. Towards automated crystallographic structure refinement with phenix.refine. *Acta Crystallogr D Biol Crystallogr* **68**, 352-67 (2012).
71. Emsley, P. & Cowtan, K. Coot: model-building tools for molecular graphics. *Acta Crystallogr D Biol Crystallogr* **60**, 2126-32 (2004).
72. DeLano, L. The PyMOL User's Manual. (DeLano Scientific
San Carlos, CA, USA., 2002).
73. Adams, P.D. et al. PHENIX: a comprehensive Python-based system for macromolecular structure solution. *Acta Crystallogr D Biol Crystallogr* **66**, 213-21 (2010).
74. Karplus, P.A. & Diederichs, K. Linking crystallographic model and data quality. *Science* **336**, 1030-3 (2012).
75. Holm, L. & Sander, C. Database algorithm for generating protein backbone and side-chain co-ordinates from a C alpha trace application to model building and detection of co-ordinate errors. *J Mol Biol* **218**, 183-94 (1991).
76. Miotto, O., Heiny, A., Tan, T.W., August, J.T. & Brusic, V. Identification of human-to-human transmissibility factors in PB2 proteins of influenza A by large-scale mutual information analysis. *BMC Bioinformatics* **9 Suppl 1**, S18 (2008).
77. Le, Q.M., Sakai-Tagawa, Y., Ozawa, M., Ito, M. & Kawaoka, Y. Selection of H5N1 influenza virus PB2 during replication in humans. *J Virol* **83**, 5278-81 (2009).
78. Manz, B., Brunotte, L., Reuther, P. & Schwemmle, M. Adaptive mutations in NEP compensate for defective H5N1 RNA replication in cultured human cells. *Nat Commun* **3**, 802 (2012).
79. Thomsen, R. & Christensen, M.H. MolDock: a new technique for high-accuracy molecular docking. *J Med Chem* **49**, 3315-21 (2006).
80. Chernov, A.A. Crystal growth and crystallography. *Acta Crystallogr A* **54**, 859-72 (1998).
81. Murshudov, G.N., Vagin, A.A. & Dodson, E.J. Refinement of macromolecular structures by the maximum-likelihood method. *Acta Crystallogr D Biol Crystallogr* **53**, 240-55 (1997).
82. Vagin, A. & Teplyakov, A. An approach to multi-copy search in molecular replacement. *Acta Crystallogr D Biol Crystallogr* **56**, 1622-4 (2000).
83. Debreczeni, J.E. & Emsley, P. Handling ligands with Coot. *Acta Crystallogr D Biol Crystallogr* **68**, 425-30 (2012).
84. van Damme, J. et al. Analysis of the catalytic site of the actin ADP-ribosylating Clostridium perfringens iota toxin. *FEBS Lett* **380**,

291-5 (1996).
85. Menetrey, J., Flatau, G., Boquet, P., Menez, A. & Stura, E.A. Structural basis for the NAD-hydrolysis mechanism and the ARTT-loop plasticity of C3 exoenzymes. *Protein Sci* **17**, 878-86 (2008).
86. Gallivan, J.P. & Dougherty, D.A. Cation-pi interactions in structural biology. *Proc Natl Acad Sci U S A* **96**, 9459-64 (1999).
87. Holmes, K.C., Popp, D., Gebhard, W. & Kabsch, W. Atomic model of the actin filament. *Nature* **347**, 44-9 (1990).
88. Kuppuraj, G., Sargsyan, K., Hua, Y.H., Merrill, A.R. & Lim, C. Linking distinct conformations of nicotinamide adenine dinucleotide with protein fold/function. *J Phys Chem B* **115**, 7932-9 (2011).
89. Jorgensen, R., Wang, Y., Visschedyk, D. & Merrill, A.R. The nature and character of the transition state for the ADP-ribosyltransferase reaction. *EMBO Rep* **9**, 802-9 (2008).
90. Hottiger, M.O., Hassa, P.O., Luscher, B., Schuler, H. & Koch-Nolte, F. Toward a unified nomenclature for mammalian ADP-ribosyltransferases. *Trends Biochem Sci* **35**, 208-19 (2010).
91. Laing, S., Unger, M., Koch-Nolte, F. & Haag, F. ADP-ribosylation of arginine. *Amino Acids* **41**, 257-69 (2011).
92. Corda, D. & Di Girolamo, M. Mono-ADP-ribosylation: a tool for modulating immune response and cell signaling. *Sci STKE* **2002**, pe53 (2002).
93. Schreiber, V. et al. Poly(ADP-ribose) polymerase-2 (PARP-2) is required for efficient base excision DNA repair in association with PARP-1 and XRCC1. *J Biol Chem* **277**, 23028-36 (2002).
94. Shniffer, A. et al. Characterization of an actin-targeting ADP-ribosyltransferase from Aeromonas hydrophila. *J Biol Chem* **287**, 37030-41 (2012).
95. Dominguez, R. Actin-binding proteins--a unifying hypothesis. *Trends Biochem Sci* **29**, 572-8 (2004).
96. Fujii, T., Iwane, A.H., Yanagida, T. & Namba, K. Direct visualization of secondary structures of F-actin by electron cryomicroscopy. *Nature* **467**, 724-8 (2010).
97. Murakami, K. et al. Structural basis for actin assembly, activation of ATP hydrolysis, and delayed phosphate release. *Cell* **143**, 275-87 (2010).
98. Pintilie, G.D., Zhang, J., Goddard, T.D., Chiu, W. & Gossard, D.C. Quantitative analysis of cryo-EM density map segmentation by watershed and scale-space filtering, and fitting of structures by alignment to regions. *J Struct Biol* **170**, 427-38 (2010).

List of Publications

1) Modification reaction mechanism based on the complex structure of enzyme-substrate protein at pre- and post-reaction states －The reaction mechanism of iota toxin from Clostridium perfringens－, Tsurumura T., Tsuge H., J of JSSRR "Housyakou", 2014 Sep: 27(5):233-240. Review in Japanese.

2) Reaction Mechanism of Mono-ADP-Ribosyltransferase Based on Structures of the Complex of Enzyme and Substrate Protein., Tsuge H, Tsurumura T., Curr Top Microbiol Immunol. 2014 Jul 3. [Epub ahead of print], Review.

3) Substrate selectivity of bacterial monoacylglycerol lipase based on crystal structure., Tsurumura T, Tsuge H., J Struct Funct Genomics. 2014 Sep;15(3):83-9. Epub 2014 Jun 4.

4) Crystallization and preliminary X-ray diffraction studies of a surface mutant of the middle domain of PB2 from human influenza A (H1N1) virus., Tsurumura T, Qiu H, Yoshida T, Tsumori Y, Tsuge H., Acta Crystallogr F Struct Biol Commun. 2014 Jan;70(Pt 1):72-5. Epub 2013 Dec 24.

5) Conformational Polymorphism of m^7GTP in Crystal Structure of the PB2 Middle Domain from Human Influenza A Virus., Tsurumura T, Qiu H, Yoshida T, Tsumori Y, Hatakeyama D, Kuzuhara T, Tsuge H., PLoS One. 2013 Nov 29;8(11):e82020.

6) Arginine ADP-ribosylation mechanism based on structural snapshots of iota-toxin and actin complex., Tsurumura T, Tsumori Y, Qiu H, Oda M, Sakurai J, Nagahama M, Tsuge H., Proc Natl Acad Sci U S A. 2013 Mar 12;110(11):4267-72. Epub 2013 Feb 4. Erratum in: Proc Natl Acad Sci U S A. 2013 Apr 30;110(18):7524.

7) Structural basis of free reduced flavin generation by flavin reductase from *Thermus thermophilus* HB8., Imagawa T, Tsurumura T, Sugimoto Y, Aki K, Ishidoh K, Kuramitsu S, Tsuge H., J Biol Chem. 2011 Dec 23;286(51):44078-85. Epub 2011 Nov 3.

8) High-Quality Protein Crystal Growth of Mouse Lipocalin-Type Prostaglandin D Synthase in Microgravity., Inaka K, Takahashi S, Aritake K, Tsurumura T, Furubayashi N, Yan B, Hirota E, Sano S, Sato M, Kobayashi T, Yoshimura Y, Tanaka H, Urade Y., Cryst Growth Des. 2011 Jun 1;11(6):2107-2111. Epub 2011 Apr 5.

9) Improvement in the quality of hematopoietic prostaglandin D synthase crystals in a microgravity environment., Tanaka H, Tsurumura T, Aritake K, Furubayashi N, Takahashi S, Yamanaka M, Hirota E, Sano S, Sato M, Kobayashi T, Tanaka T, Inaka K, Urade Y., J Synchrotron Radiat. 2011 Jan;18(1):88-91. Epub 2010 Nov 5.

10) High-quality crystals of human haematopoietic prostaglandin D synthase with novel inhibitors., Takahashi S, Tsurumura T, Aritake K, Furubayashi N, Sato M, Yamanaka M, Hirota E, Sano S, Kobayashi T, Tanaka T, Inaka K, Tanaka H, Urade Y., Acta Crystallogr Sect F Struct Biol Cryst Commun. 2010 Jul 1;66(Pt 7):846-50. Epub 2010 Jun 24.

11) Structural basis for the *Helicobacter pylori*-carcinogenic TNF-alpha-inducing protein., Tsuge H, Tsurumura T, Utsunomiya H, Kise D, Kuzuhara T, Watanabe T, Fujiki H, Suganuma M., Biochem Biophys Res Commun. 2009 Oct 16;388(2):193-8. Epub 2009 Jul 28.

12) Structural basis of the catalytic mechanism operating in open-closed conformers of lipocalin type prostaglandin D synthase., Kumasaka T, Aritake K, Ago H, Irikura D, Tsurumura T, Yamamoto M, Miyano M, Urade Y, Hayaishi O., J Biol Chem. 2009 Aug 14;284(33):22344-52. Epub 2009 Jun 22.

13) NMR solution structure of lipocalin-type prostaglandin D synthase: evidence for partial overlapping of catalytic pocket and retinoic acid-binding pocket within the central cavity., Shimamoto S, Yoshida T, Inui T, Gohda K, Kobayashi Y, Fujimori K, Tsurumura T, Aritake K, Urade Y, Ohkubo T., J Biol Chem. 2007 Oct 26;282(43):31373-9. Epub 2007 Aug 22. Erratum in: J Biol Chem. 2008 Mar 28;283(13):8772.

Acknowledgement

The author sincerely wishes to express his special gratitude to Prof. Hideaki TSUGE for his enthusiastic guidance, helpful suggestion, stimulating discussion and continuous encouragement.

In Chapter I, the author appreciates to Ms. Hiroko UTSUNOMIYA (Institute for Health Sciences, Tokushima Bunri University) for her generous and continuous support. The author is also grateful to Mr. Daisuke KISE, Prof. Takashi KUZUHARA and Prof. Hirota FUJIKI (Faculty of Pharmaceutical Sciences, Tokushima Bunri University) and Tatsuro WATANABE, Ms. Kaori SUZUKI, Ms. Miki KURUSU, Ikuko SHIOTANI and Masami SUGANUMA (Research Institute for Clinical Oncology, Saitama Cancer Center) for their stimulating and continuous discussions.

This work was supported in part by the following Grantsin-Aid for Scientific Research from the Ministry of Education, Culture, Sports, Science and Technology (MEXT) of Japan, the Academic Frontier Promotion Program of MEXT of Japan, the Japan Society for the Promotion of Science, and the Smoking Research Fund.

In Chapter II, the author appreciates to Dr. Dai HATAKEYAMA and Prof. Takashi KUZUHARA (Faculty of Pharmaceutical Sciences, Tokushima Bunri University) for their stimulating discussions for this work. The author also appreciates to Prof. Nobuo SHIMAMOTO and Dr. Hideki NAKAYAMA for the advice on a subcloning technique.

The influenza (A/PR/8/34) RNA polymerase PB2 plasmid, pBMSA-PB2, was provided by the DNA Bank, RIKEN BioResource Center (Tsukuba, Japan; originally deposited by Dr. Susumu Nakada) with the support of National Bio-Resources Project of the MEXT.

In Chapter III, the author appreciates to Dr. Masataka ODA, Prof. Jun SAKURAI and Prof. Masahiro NAGAHAMA (Faculty of Pharmaceutical Sciences, Tokushima Bunri University) for their stimulating discussions for this work.

This work was supported in part by a Strategic Research Foundation Grant-Aided Project for Private Universities; by the Ministry of Education, Culture, Sports, Science and Technology (MEXT) of Japan; and by Grants-in-Aid for Scientific Research, MEXT of Japan.

In all of these works, the author thanks to KEK and SPring-8 staffs for their kindly support with data collection.

Special thanks are given to author's colleagues at work, Dr. Toru YOSHIDA, and Ms. Hao QIU. Especially, the author thanks to Ms. Yayoi TSUMORI for totally technical support.

Finally, the author wishes to express his thanks to his family, especially my wife Sayuri for her understanding and hearty encouragement.

Toshiharu TSURUMURA